minerals

MDPI

Article

Experimental Modeling of Mantle Metasomatic Processes Involving Carbon- and Sulfur-Bearing Agents in an Olivine–Siderite–Sulfur System at Early-Subduction Mantle Conditions

Yuliya V. Bataleva and Yuri N. Palyanov *

V.S. Sobolev Institute of Geology and Mineralogy, Siberian Branch of Russian Academy of Sciences, Koptyug Ave 3, Novosibirsk 630090, Russia; bataleva@igm.nsc.ru
* Correspondence: palyanov@igm.nsc.ru; Tel.: +7-383-373-05-26

Abstract

During Precambrian subduction, banded iron formations (BIFs) may have represented an early significant input of carbonates and atmospheric sulfur into the lithospheric mantle, initiated the formation of carbonatite melts and probably triggered mantle metasomatic processes. Experimental modeling of the interaction of BIF-related metasomatic agents with upper mantle rocks, under Archean subduction geotherm, was performed in the simplified olivine–siderite–sulfur system. Experiments were carried out at 6.3 GPa, temperature range of 1150–1450 °C and durations of 20–60 h, using a multi-anvil high-pressure apparatus of a "split-sphere" type. Interaction of Fe,Ni–olivine and siderite with sulfur melt leads to the formation of pyrrhotite + orthopyroxene + ferromagnesite ± magnetite assemblage (1150–1250 °C, 40–60 h), as well as generation of sulfide (1350–1450 °C) and carbonate–silicate melts (1450 °C, 20 h); in all experiments, dissolution of diamond seed crystals is observed. Redox conditions are estimated to approximately correspond to fO_2 ~ CCO + 0.5 log. units. We demonstrated that during experiments, sulfidation of Fe,Ni–olivine and siderite and redox dissociation of siderite took place. It was shown that indicators of these processes are (1) polycrystalline orthopyroxene + pyrrhotite and pyrrhotite + ferromagnesite aggregates, inheriting shape of olivine and siderite crystals, respectively; (2) orthopyroxene zoned crystals with pyrrhotite inclusions; (3) pyrrhotite with ferromagnesite inclusions and ferromagnesite with magnetite + pyrrhotite inclusions. The obtained results with certain limitations can be used to constrain processes of metasomatic alteration of upper mantle rocks by agents enriched in iron, sulfur, and carbon under relatively oxidizing conditions (fO_2 ~ CCO + 0.5 log. units).

Keywords: high-pressure experiment; mantle metasomatism; experimental modeling; diamond dissolution; sulfidation; mantle sulfides

Check for updates

Academic Editor: Paris Xypolias

Received: 28 June 2026
Revised: 30 July 2026
Accepted: 9 August 2026
Published: 12 August 2026

Copyright: © 2026 by the authors. Licensee MDPI, Basel, Switzerland. This article is an open access article distributed under the terms and conditions of the Creative Commons Attribution (CC BY) license.

1. Introduction

According to modern concepts, subduction processes are supposed to have started approximately 3 billion years ago in the Mesoarchean [1–3]. During this time and continuing into the Paleoproterozoic (up to 1.8 billion years ago), unique sedimentary rocks, banded iron formations (BIFs), formed in marine basins, primarily in shallow coastal waters and on shelves [4,5]. Banded iron formations were composed of alternating layers of iron oxides and cherts, often also containing ferrous carbonates (siderite or ankerite, up to 50 vol.%),

iron sulfides (up to 15 vol.%), and carbonaceous shales [4,6–10]. The total FeO + Fe_2O_3 content in BIFs could reach 85 wt.%. As ocean basin sediments, they were subducted deep into the Earth during early subduction. In one possible geological scenario, down-going slabs, transporting banded iron formations and recycled altered Earth's crust, could be the first significant inputs of atmospheric sulfur (as S_2–S_8 and H_2S fluid components and sedimentary pyrite) and carbonates into the mantle, initiating the formation of carbonate–silicate and carbonatite melts and triggering metasomatic processes in the slab, mantle wedge, and lithospheric mantle [11–14]. For example, subduction of a 500-m BIF (as in Hamersley, Australia) with only 1 wt.% of siderite has been recognized to result in a metasomatized layer of a few kilometers thick above the subduction interface [12].

Carbonatite melts, originated from subducted BIFs, as well as components of C–O–H–S fluids, originated from a recycled altered Earth's crust, can be considered as simplified model compositions of metasomatic agents that could have formed during early subduction. In bulk, these fluids/melts are enriched in iron, sulfur, and carbon, the main redox-sensitive elements of the Earth's interior, having a strong impact on the redox evolution of the mantle and the redox budget of subduction zones [15].

Despite the current high relevance of theoretical and experimental studies of mantle metasomatism, very few of them address processes that occurred in the Earth's early history. We believe that modeling the first metasomatic transformations in the mantle involving subducted BIFs can shed light on the indicator characteristics of the metasomatic alterations of ultramafic rocks in the mantle wedge by agents enriched in iron, sulfur, and carbon. To achieve this goal, it seems relevant to conduct an experimental study of the interaction in the Fe,Ni–olivine–siderite–sulfur system, which, in a simplified form, models the interaction of BIF-related metasomatic agents with ultramafic rocks of the Archean upper mantle, under conditions corresponding to the model Archean subduction temperatures [16–18], which were at least 200 °C warmer than today. It should be noted that previously we have experimentally studied interactions in olivine–magnesite–sulfur, olivine–ankerite–sulfur, and olivine–ankerite–pyrite systems, simulating metasomatic transformations of carbonate-silicate associations under the influence of sulfur-enriched melts/fluids [19,20], and identified indicators of these processes.

As it was mentioned above, Fe,Ni–olivine–siderite–sulfur system is simplified and has a number of limitations. First, this system does not include major BIF-forming minerals, such as Fe–oxide and quartz/chert; only siderite and sulfur were used to model composition of S,C-rich metasomatic agents, supposedly formed as a result of the melting of banded iron formations. Real composition of these agents under natural conditions is much more complex. Since our experimental study is the first in this area, we use a simplified system to determine the role of each phase (carbonate/carbonate melt, S-rich fluid or melt, olivine) and explore scenarios of how these phases interact with each other. The second limitation is that only olivine was used to model ultramafic rocks of the upper mantle. According to published data, olivine composition in the Archaean mantle was in the range of 91.5–94% forsterite component [21–24]. As a first approximation, olivine within this compositional range can be used as a simplified mantle component.

2. Materials and Methods

2.1. Experimental Approach

The experiments were conducted using multi-anvil high-pressure apparatus of a "split-sphere" type (BARS) (non-serial, Novosibirsk, Russian Federation) [25] with a high-pressure cell (tetragonal prism 21.1 × 21.1 × 25.4 mm). The main feature of the cell is its relatively large volume, which enables comprehensive analytical studies of the obtained samples. The cell configuration and heater geometry (height 25.4 mm, length 14.8 mm, inner diameter 9

mm) provide a low-gradient zone in the center of the cell, where the graphite capsule containing the sample was positioned. The temperature contrast recorded in the low-gradient cell zone gives an error ± 17 °C (Figure 1 in [26]). The details of the P,T-parameters (pressure and temperature) calibration are presented in [26–28]. The pressure was recorded by the change in the resistance of the reference substances Bi (2.55 GPa) and PbSe (4.0 and 6.8 GPa) at room temperature, followed by the construction of calibration curves and their reference at high temperature to the graphite–diamond equilibrium line [29,30]. Temperature measurement and control during the experiments were carried out using thermocouples made of $PtRh_6/PtRh_{30}$ (Yekaterinburg Non-ferrous metal Processing Plant, Yekaterinburg, Russian Federation) and placed inside high-pressure cells. Accuracy of the pressure and temperature measurements was at the level of ± 0.1 GPa and ± 20 °C [28]. The samples were heated up at a rate of ~0.5 °C/s. Rapid quenching of the samples (150–200 °C/sec) was carried out to ensure detailed study of the melts compositions. It is supposed the bulk composition of the quenched aggregates obtained by rapid quenching adequately reflects the composition of the melts generated under the P,T-parameters of the experiments.

2.2. Starting Materials

Experimental modeling of the interaction of BIF-related metasomatic agents with upper mantle rocks, under Archean subduction geotherm, was performed in the simplified olivine–siderite–sulfur system ($(Mg,Fe,Ni)_2SiO_4$–$(Fe,Mg,Ca,Mn)CO_3$–S). Experiments were carried out at a pressure of 6.3 GPa, in the temperature range of 1150–1450 °C, and at durations of 20 to 60 h. At lower temperatures, run durations were systematically increased (e.g., 60 h at 1150 °C vs. 20 h at 1450 °C) to compensate slower kinetics, lower chemical reaction rates as well as diffusion rates.

Natural olivine ($Mg_{1.8}Fe_{0.19}Ni_{0.01}SiO_4$) from a xenolith of granular spinel lherzolite from the Udachnaya kimberlite pipe (Yakutia), natural siderite ($Fe_{0.84}Mg_{0.08}Ca_{0.04}Mn_{0.04}CO_3$, Saint-Pierre-de-Mésage, France), and elemental sulfur (99.99% purity) (JSC LenReactiv, Saint-Petersburg, Russian Federation) were used as initial reagents. The compositions of the initial materials and the bulk composition of the system are given in Table 1, and the weights of the initial reagents are given in Table 2. These tables also contain data on our previously conducted experiments in the olivine–carbonate–sulfur and olivine–carbonate–sulfide systems [19,20] for comparison. In all olivine–carbonate–sulfur systems, the weight proportions of Fe,Ni–olivine and sulfur, as well as carbon content, were constant. Weights of carbonates in each system were different because of differences in densities and molar weights between magnesite, ankerite, and siderite. The olivine/sulfur ratio was chosen in accordance with the stoichiometry of the schematic reaction Mg,Fe,Ni–olivine + sulfur → Mg-olivine + Mg-orthopyroxene + pyrrhotite to achieve complete extraction of transition metals from olivine to form pyrrhotite.

Table 1. Compositions of initial olivine and carbonates, as well as the bulk compositions of the olivine–carbonate–sulfur and olivine–carbonate–sulfide systems we studied earlier [19,20].

Mineral/Bulk System	Composition, wt.%								
	Si	Fe	Mg	Ca	Mn	Ni	S	C	O
Fe,Ni–olivine	19.1	7.2	29.6	-	-	0.4	-	-	43.7
Siderite	-	41.7	1.7	1.4	2.0	-	-	10.6	42.6
Olivine–siderite–sulfur	7.3	23.9	12.2	0.7	1.0	0.2	10.9	5.4	38.4
Olivine–magnesite–sulfur [19]	8.6	3.3	23.8	1.9	0.0	0.2	13.7	5.7	42.8
Olivine–ankerite–sulfur [20]	8.4	9.2	15.5	8.5	0.2	0.2	12.5	5.3	40.3
Olivine–ankerite–pyrite [20]	8.3	15.5	15.3	8.3	0.2	0.2	7.3	5.2	39.7

Table 2. Weights of the starting materials in the olivine–siderite–sulfur system, as well as in the olivine–carbonate–sulfur and olivine–carbonate–sulfide systems, which we studied earlier [19,20].

System	Weights, mg						
	Ol	Ms	Dol	Ank	Sd	S	Py
Olivine–siderite–sulfur	30.0	–	–	–	39.6	8.5	–
Olivine–magnesite–sulfur [19]	28.0	20.0	5.4	–	–	8.5	–
Olivine–ankerite–sulfur [20]	30.0	–	–	30.0	–	8.5	–
Olivine–ankerite–pyrite [20]	33.2	–	–	33.0	–	–	10.5

Ol—olivine, Ms—magnesite, Dol—dolomite, Ank—ankerite, Sd—siderite, S—sulfur, Py—pyrite.

Initial reagents were finely ground (10–20 μm), thoroughly mixed, and then placed in graphite capsules (Chelyabinsk Electrode Plant, Chelyabinsk, Russian Federation). Graphite was chosen as the optimal capsule material based on previous experience with sulfides and sulfur under mantle pressures and temperatures [31]. It was estimated in our previous studies [19,20] that the graphite capsules with thick walls maintains oxygen fugacity in carbonate-bearing samples near the CCO (C-CO) buffer. Three seed synthetic diamond crystals of cuboctahedral habit (Element Six, Shannon, Ireland), ~500 μm in size, were placed in each sample to obtain information on diamond growth or dissolution under the experimental parameters, as well as an additional indicator whether oxygen fugacity values were below or above CCO buffer.

2.3. Analytical Studies

After experiments samples were vertically sawn into two equal halves: one was impregnated with epoxy resin and polished, while the diamond seed crystals were extracted from the other half, and the cleaved surfaces were prepared for further analytical studies. Initial examination of the samples was performed using a Stemi 508 (Carl Zeiss Microscopy, Jena, Germany) and Axio Imager Z2m stereomicroscopes (Carl Zeiss Microscopy, Jena, Germany; ZEISS ZEN core version 3.13 software). The phase and chemical compositions of the samples were studied using microprobe analysis (Jeol JXA-8100, JEOL Ltd., Tokyo, Japan), scanning electron microscopy, and energy-dispersive spectroscopy (TESCAN MIRA 3 LMU, Tescan, Brno, Czech Republic; TESCAN control software version 4.1). Silicate phases were analyzed at an accelerating voltage of 20 kV, a probe current of 20 nA, a counting time of 10 s for each analytical line, and an electron beam probe diameter of 2–4 μm. As standards we used olivine CH-1 (MgO, FeO, and SiO_2), IGEM (MnO), spinel NIFE204 (NiO), and diopside DIOPSIDE (CaO). The error in component determination by microprobe analysis did not exceed 0.2 wt%. To analyze the compositions of quenched melts, which are represented by microdendritic aggregates, the electron beam diameter was increased to 20–50 μm. The increased beam diameter allowed for area recording, and averaged compositions of the quenched microdendritic aggregates were obtained. It should be noted that this technique is associated with high error; however, it is widely used in experimental studies [32–34], as no alternatives currently exist.

To study the morphology of diamond seed crystals, differential interference contrast microscopy (Axio Imager Z2m microscope, Carl Zeiss Microscopy, Jena, Germany) and scanning electron microscopy were used. Raman spectroscopy was used to study the structural features of silicates, carbonates, sulfides, oxides, and graphite (Jobin Yvon LabRAM HR800 spectrometer, Horiba, Tokyo, Japan (LabSpec 6 software, HORIBA Scientific, Tokyo, Japan), equipped with an Olympus BX41 stereo microscope, Horiba Jobin Yvon S.A.S., Lonjumeau, France (cellSens Imaging software, Evident, Tokyo, Japan)). A He-Cd laser (Kimmon Koha Co., Ltd., Tokyo, Japan) with a wavelength of 325 nm was used as an excitation source. Analytical studies were carried out at the V.S. Sobolev Institute of Geology

and Mineralogy SB RAS and the Center for Collective Use of Multi-element and Isotopic Analysis of the Siberian Branch of Russian Academy of Sciences.

3. Results

3.1. Results of Experiments Carried out in the Olivine–Siderite–Sulfur System

Experimental parameters and results are presented in Table 3. At the lowest temperature and the longest run duration (1150 °C, 60 h), an association of pyrrhotite, orthopyroxene, ferromagnesite, and magnetite, as well as single grains of recrystallized olivine, is formed. These mineral phases are distributed relatively uniformly throughout the reaction volume. The general structure of the sample is shown in Figure 1a. It is found that in general, pyrrhotite in the obtained samples occurs in direct contact with ferromagnesite. More specifically, ferromagnesite contains pyrrhotite inclusions (Figure 2a–f) and vice versa (Figure 2g–i), pyrrhotite and ferromagnesite form specific polycrystalline aggregates (Figure 2g,h), and pyrrhotite crystals are surrounded by ferromagnesite rims (Figure 2g,h). The composition of the obtained pyrrhotite within the sample is constant and corresponds to the formula $Fe_{0.93–0.95}Ni_{0.01}S$ (Table 4).

Ferromagnesite in the samples is present as relatively large crystals (40–100 μm) (Figure 2a–d). Its Raman characteristics are shown in Figure 3. These crystals often contain inclusions of magnetite, pyrrhotite, and sometimes orthopyroxene (Figure 2a–f). Magnetite inclusions are typically spherical or rounded, some of these inclusions are two-phase and contain a magnetite + pyrrhotite association (Figure 2b–f). Magnetite inclusions are located in groups, which are confined to the central parts of ferromagnesite crystals.

Table 3. Parameters and results of experiments carried out in the olivine–siderite–sulfur, olivine–magnesite–sulfur [19], olivine–ankerite–sulfur [20] and olivine–ankerite–pyrite [20] systems (at a pressure of 6.3 GPa).

Run N	System	*T* (°C)	*t* (hrs)	Final Phases
E-76	Olivine–siderite–sulfur	1150	60	Opx, Fms, Mgt, Po, Ol
E-97		1250	40	Opx, Fms, Po
E-00		1350	20	Opx, Fms, L_{sulf}
E-01		1450	20	Opx, Fms, L_{sulf}, $L_{carb-sil}$
OCS-6	Olivine–magnesite–sulfur [19]	1150	40	Ol, Opx, Ms, Py, L_s
OCS-2		1250	40	Ol, Opx, Ms, Py, L_s
OCS-9		1350	40	Ol, Opx, Ms, L_s
OCS-8		1450	40	Ol, Opx, Ms, L_s, L_{carb}
1476-3	Olivine–ankerite–sulfur [20]	1150	60	Ol, Cpx, Dol, Ms, Arg, Py, L_s
1997-3		1250	60	Ol, Cpx, Dol, Ms, Py, L_s
2000-3		1350	20	Ol, Cpx, Dol, Ms, L_s, Gr
2001-3		1450	20	Ol, Opx, Dol, Ms, $L_{carb-sil}$, L_s, Gr
1476-6	Olivine–ankerite–pyrite [20]	1150	60	Ol, Cpx, Dol, Ms, Py, Po
1997-6		1250	60	Ol, Cpx, Dol, Ms, Py, Po
2000-6		1350	20	Ol, Cpx, Dol, Ms, L_{carb}, L_{Fe-S-O}
2001-6		1450	20	Ol, Cpx, Ms, L_{carb}, L_{Fe-S-O}, Gr

Ol—olivine (recrystallized), Opx—orthopyroxene, Cpx—clinopyroxene, Fms—ferromagnesite, Ms—magnesite, Dol—dolomite, Arg—aragonite, Py—pyrite, Po—pyrrhotite, Mgt—magnetite, L_s—sulfur melt with variable concentrations of dissolved Fe, Ni and O, L_{carb}—carbonate melt, $L_{carb-sil}$—carbonate-silicate melt, L_{Fe-S-O}—sulfide melt with dissolved oxygen, L_{sulf}—sulfide melt, Gr—graphite.

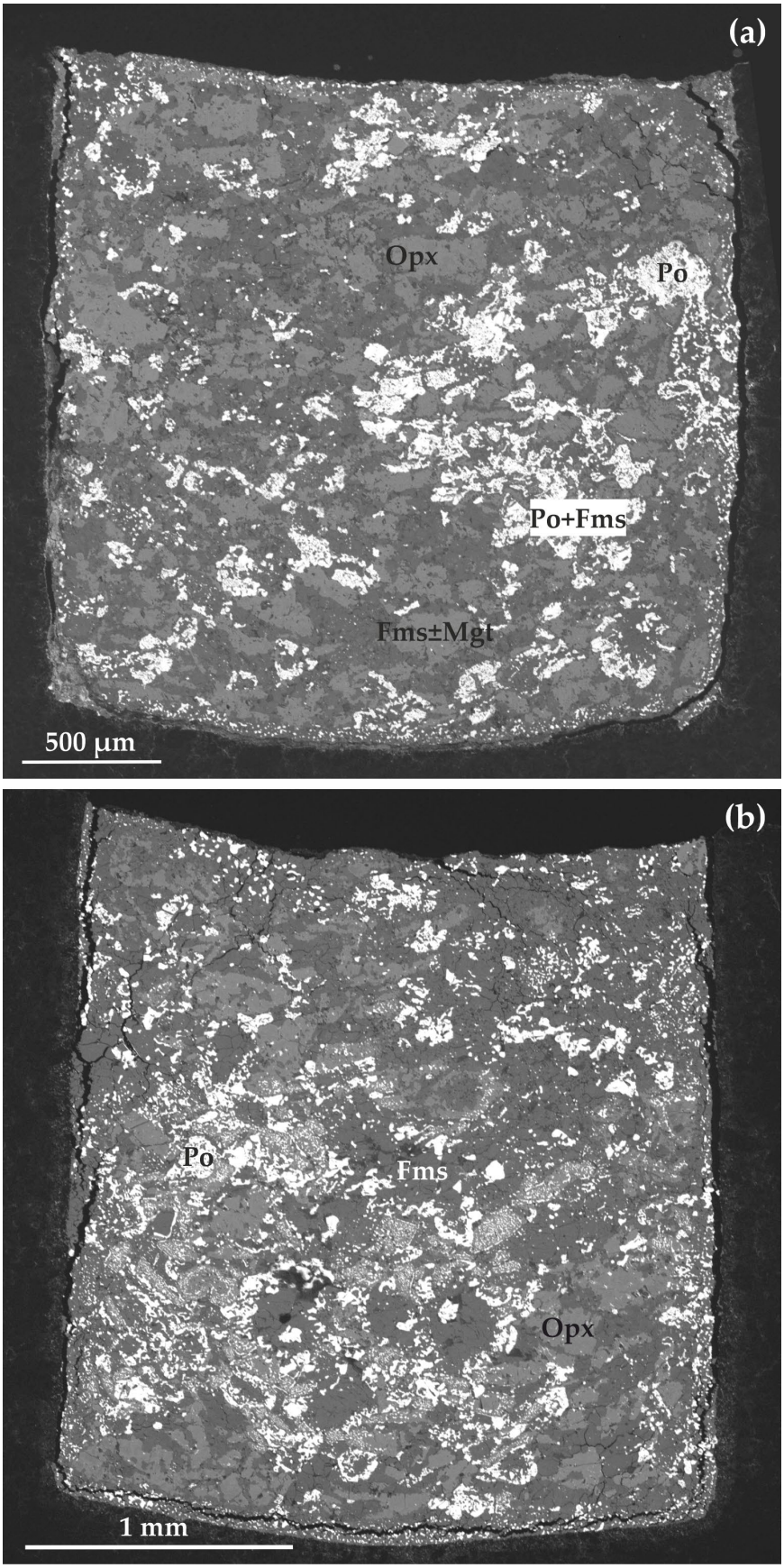


Figure 1. SEM micrographs (BSE regime) of polished vertical sections of the samples: (**a**) run E-76, 1150 °C; (**b**) run E-97, 1250 °C; Opx—orthopyroxene, Fms—ferromagnesite, Po—pyrrhotite, Mgt—magnetite.

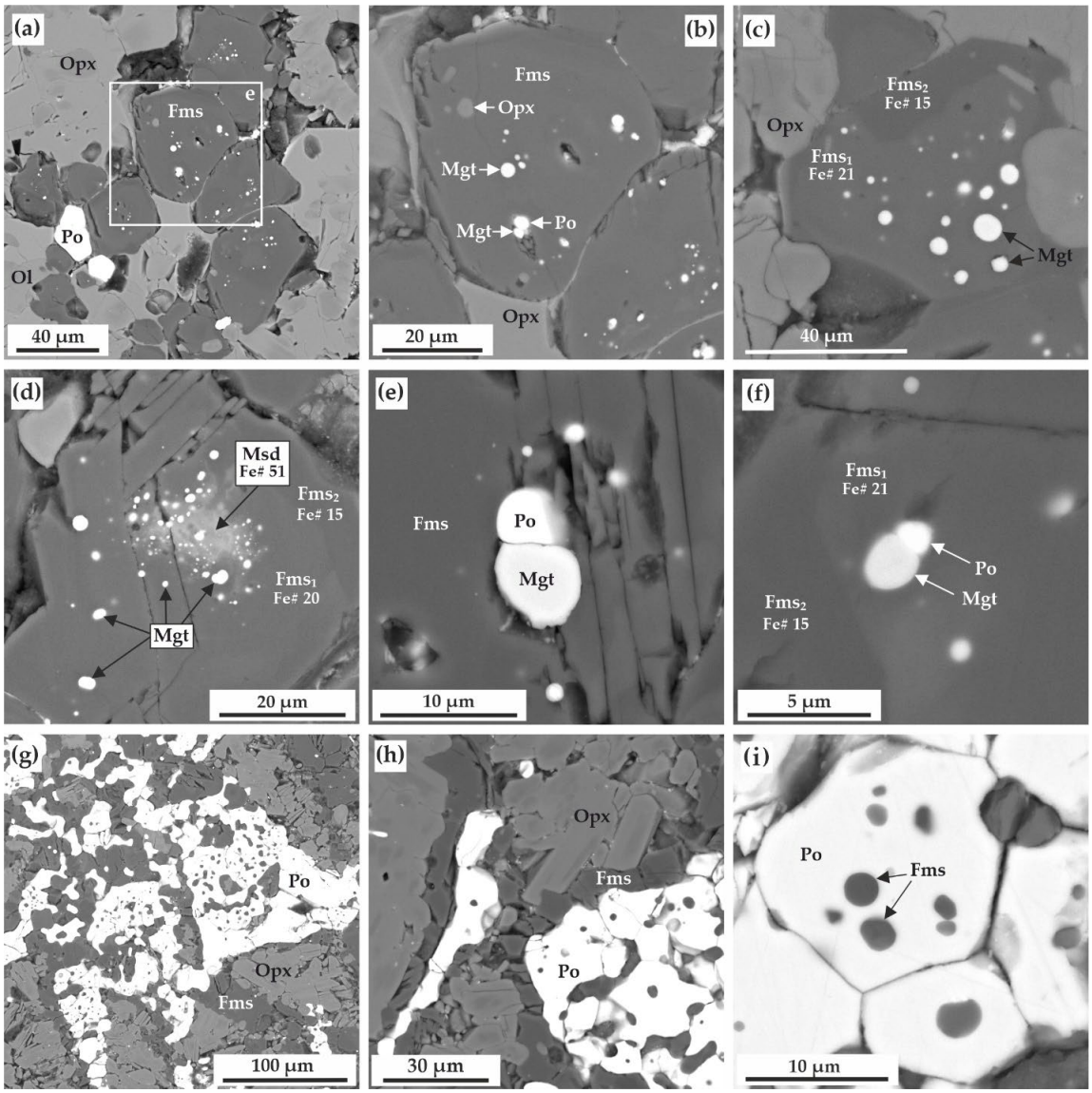


Figure 2. SEM micrographs (BSE regime) of polished sections of the samples, after experiments in olivine–siderite–sulfur under 6.3 GPa, 1150 °C, 60 h (run E-76): (**a**) polycrystalline aggregate of orthopyroxene, ferromagnesite, pyrrhotite as well as recrystallized olivine; (**b**) enlarged fragment of (**a**), inclusions of magnetite, pyrrhotite and orthopyroxene in ferromagnesite; (**c**,**d**) magnetite inclusions in zoned ferromagnesite crystals; (**e**,**f**) two-phase inclusions of magnetite and pyrrhotite in ferromagnesite crystals; (**g**,**h**) polycrystalline aggregate of orthopyroxene, ferromagnesite, and pyrrhotite; (**i**) ferromagnesite inclusions in pyrrhotite. Ol—recrystallized olivine, Opx—orthopyroxene, Fms—ferromagnesite, Msd—magnesiosiderite, Po—pyrrhotite, Mgt—magnetite, Fe#—Fe/(Fe + Mg + Ca + Mn), molar.

Table 4. Compositions of sulfide phases after experiments in olivine–siderite–sulfur system (6.3 GPa).

Run N	*T* (°C)	Phase	Mass Concentrations, wt.%				Atomic Concentrations, at. %				Formula Units		
			Fe	Ni	S	Total	Fe	Ni	S	Total	Fe	Ni	S
E-76	1150	Po	61.9	0.7	37.3	99.9	48.4	0.5	51.0	100.0	0.95	0.01	1
			61.7	0.7	37.4	99.7	48.3	0.5	51.2	100.0	0.94	0.01	1
			61.4	0.7	37.5	99.6	48.1	0.5	51.4	100.0	0.94	0.01	1
			61.4	0.7	37.7	99.8	48.0	0.5	51.5	100.0	0.93	0.01	1
		Mean, 24	$61.9_{(4)}$	$0.7_{(1)}$	$37.7_{(3)}$	100.4	$48.1_{(6)}$	$0.6_{(1)}$	$51.3_{(3)}$	100.0	$0.94_{(1)}$	$0.01_{(0)}$	1

Table 4. *Cont.*

Run N	*T* (°C)	Phase	Mass Concentrations, wt.%				Atomic Concentrations, at. %				Formula Units		
			Fe	Ni	S	Total	Fe	Ni	S	Total	Fe	Ni	S
E-97	1250	Po	60.5	0.7	39.4	100.6	46.5	0.5	53.0	100.0	0.88	0.01	1
			60.2	0.5	39.3	100.0	46.5	0.4	53.1	100.0	0.88	0.01	1
			59.5	0.7	39.2	99.4	46.2	0.5	53.3	100.0	0.87	0.01	1
			59.9	0.6	39.4	99.9	46.2	0.5	53.3	100.0	0.87	0.01	1
			60.4	0.6	39.5	100.5	46.4	0.4	53.1	100.0	0.87	0.01	1
		Mean, 25	$60.4_{(5)}$	$0.7_{(1)}$	$39.5_{(4)}$	100.5	$46.4_{(4)}$	$0.5_{(2)}$	$53.1_{(1)}$	100.0	$0.87_{(0)}$	$0.01_{(0)}$	1
E-00	1350	L_{sulf}	60.7	0.7	38.5	99.9	47.1	0.5	52.4	100.0	-	-	-
			60.6	0.7	38.5	99.7	47.1	0.5	52.4	100.0	-	-	-
			61.1	0.6	38.3	100.0	47.5	0.4	52.1	100.0	-	-	-
			60.7	0.8	38.3	99.9	47.3	0.6	52.1	100.0	-	-	-
			61.1	0.8	38.6	100.5	47.2	0.6	52.2	100.0	-	-	-
			60.8	0.6	38.6	99.9	47.2	0.4	52.4	100.0	-	-	-
		Mean, 28	$60.7_{(4)}$	$0.7_{(1)}$	$38.3_{(4)}$	99.7	$47.2_{(5)}$	$0.5_{(1)}$	$52.3_{(2)}$	100.0	-	-	-
E-01	1450	L_{sulf}	60.3	0.6	38.6	99.5	46.9	0.5	52.6	100.0	-	-	-
			60.1	0.7	38.9	99.8	46.6	0.5	52.8	100.0	-	-	-
			60.2	0.7	38.9	99.8	46.7	0.5	52.8	100.0	-	-	-
			60.3	0.6	38.7	99.6	46.9	0.4	52.7	100.0	-	-	-
			60.2	0.6	38.7	99.5	46.8	0.5	52.7	100.0	-	-	-
			60.1	0.6	38.5	99.3	46.9	0.5	52.6	100.0	-	-	-
			60.2	0.7	38.5	99.4	46.9	0.5	52.6	100.0	-	-	-
			60.3	0.8	38.8	99.9	46.8	0.6	52.7	100.0	-	-	-
		Mean, 33	$60.5_{(4)}$	$0.7_{(1)}$	$38.5_{(4)}$	99.6	$46.8_{(9)}$	$0.5_{(3)}$	$52.7_{(3)}$	100.0	-	-	-

Po—pyrrhotite, L_{sulf}—sulfide melt, mean—averaged compositions of sulfide phases ("Mean, 33" should be read as averaged compositions calculated based on 33 analyses); the values in parentheses are one sigma errors of the means based on replicate electron microprobe analyses reported as least units cited; $60.5_{(4)}$ should be read as 60.5 ± 0.4 wt.%.

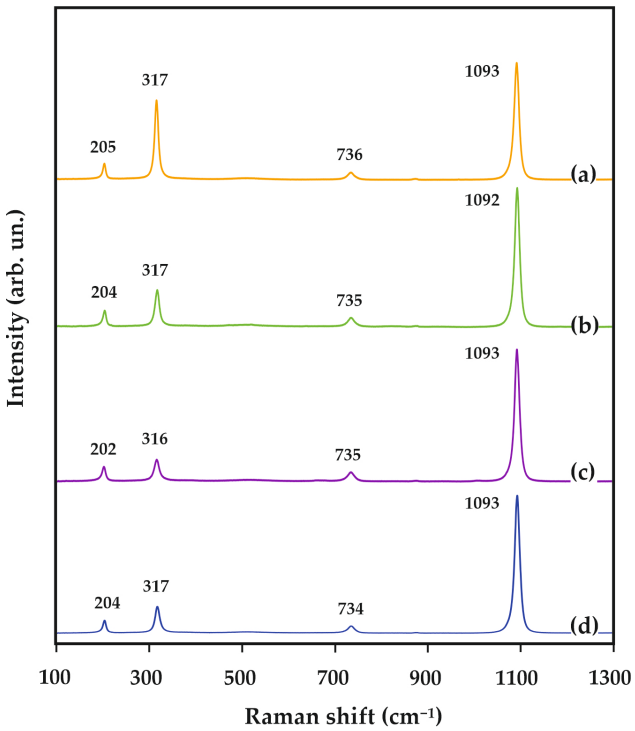


Figure 3. Representative Raman spectra of newly formed ferromagnesite: (**a**) run E-76, 1150 °C; (**b**) run E-97, 1250 °C; (**c**) run E-00, 1350 °C; (**d**) run E-01, 1450 °C; arb. un. arbitrary unit.

It should be emphasized that magnetite in the samples is present only as inclusions in ferromagnesite. Impurities of SiO_2 (1.4–2.3 wt.%), MgO (2.1–17.5 wt.%), and MnO

(0.8–1.2 wt.%) have been established for magnetite (Table 5). Ferromagnesite crystals with magnetite inclusions are characterized by zoning, in which the central part is enriched in FeO and MnO, and the peripheral part, on the contrary, is enriched in magnesium and calcium (Figure 2c,d,f). In the vast majority of cases, ferromagnesite crystals contain two zones separated by a sharp boundary (Figure 2c,d,f), with the concentrations of FeO in the central part being 15–16 wt.% and CaO being 0.4–0.6 wt.%, and in the peripheral part, FeO is 11–12 wt.% and CaO is 1.2–1.3 wt.% (Table 6, Figure 4).

Table 5. Compositions of oxide phases after experiments in olivine–siderite–sulfur system (6.3 GPa and 1150 °C).

Run N	Phase	Mass Concentrations, wt.%							Cations per Formula Unit, p.f.u.					
		SiO_2	FeO *	FeO_{calc}	$Fe_2O_{3\ calc}$	MnO	MgO	Total *	Si	Mn	Mg	Fe^{2+}_{calc}	Fe^{3+}_{calc}	Total
E-76	Mgt	2.3	84.5	25.9	65.1	0.8	4.6	92.1	0.09	0.03	0.25	0.81	1.83	3.00
		2.0	87.9	28.5	66.0	0.7	2.9	93.4	0.07	0.02	0.16	0.89	1.85	3.00
		1.8	85.9	24.3	68.4	0.9	5.5	94.1	0.07	0.03	0.30	0.74	1.87	3.00
		1.4	88.9	28.8	66.8	1.0	2.1	93.4	0.05	0.03	0.12	0.91	1.89	3.00
	Mfr	1.4	69.9	9.2	67.4	1.1	13.0	85.4	0.05	0.04	0.73	0.29	1.90	3.00
		1.7	70.3	4.5	73.0	1.2	17.5	90.5	0.06	0.03	0.89	0.13	1.89	3.00

Mgt—magnetite, Mfr—magnesioferrite; number of cations p.f.u. was calculated per 4 oxygen atoms; *—values according to initial analyses; calc—calculated values.

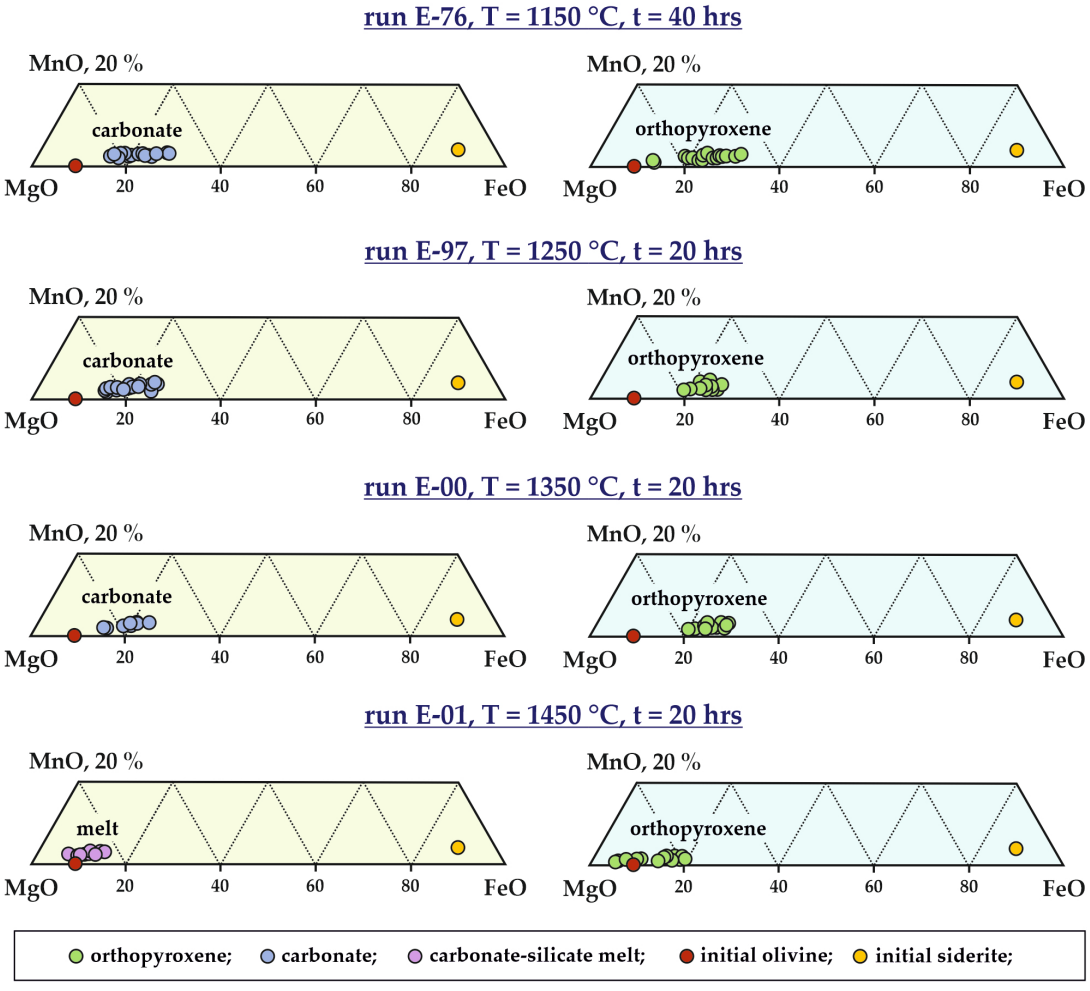


Figure 4. Compositional diagrams of orthopyroxene, carbonate, and carbonate–silicate melt.

Table 6. Compositions of carbonate phases after experiments in olivine–siderite–sulfur system.

Run N	Phase	Mass Concentrations, wt.%								Cations per Formula Unit, p.f.u.						
		SiO_2	FeO	MnO	MgO	CaO	SO_3	CO_2 *	Total	Fe	Mn	Mg	Ca	C	Total	Fe#
E-76	Fms	-	12.2	2.1	36.4	1.2	-	48.2	100.0	0.15	0.03	0.82	0.02	0.99	2.01	0.15
		-	14.9	1.9	34.7	-	-	48.5	100.0	0.19	0.02	0.79	0.00	1.00	2.00	0.19
		-	16.6	2.1	33.9	0.2	-	47.3	100.0	0.21	0.03	0.78	0.00	0.99	2.01	0.21
		-	18.9	2.2	31.7	0.4	-	46.8	100.0	0.25	0.03	0.74	0.01	0.99	2.01	0.24
		-	21.3	2.4	29.9	0.3	-	46.1	100.0	0.28	0.03	0.71	0.01	0.99	2.01	0.27
		-	36.1	3.2	16.0	0.4	-	44.3	100.0	0.51	0.05	0.40	0.01	1.02	1.98	0.53
	Mean	-	$16.5_{(25)}$	$2.2_{(21)}$	$33.4_{(17)}$	$0.5_{(4)}$	-	$47.4_{(10)}$	100.0	$0.21_{(3)}$	$0.03_{(0)}$	$0.77_{(3)}$	$0.01_{(1)}$	$0.99_{(1)}$	$2.01_{(1)}$	0.21
E-97	Fms	-	11.4	1.9	36.1	1.0	-	49.6	100.0	0.14	0.02	0.81	0.02	1.01	1.99	0.14
		-	12.5	2.0	35.4	0.8	-	49.3	100.0	0.16	0.02	0.79	0.01	1.01	1.99	0.16
		-	14.6	1.6	34.9	1.1	-	47.8	100.0	0.19	0.02	0.79	0.02	0.99	2.01	0.18
		-	16.3	2.8	32.9	0.7	-	47.3	100.0	0.21	0.03	0.76	0.01	0.99	2.01	0.21
		-	17.0	2.3	33.6	-	-	47.0	100.0	0.22	0.03	0.78	0.00	0.99	2.01	0.21
		-	19.2	1.6	32.2	-	-	46.9	100.0	0.25	0.02	0.75	0.00	0.99	2.01	0.24
	Mean	-	$15.2_{(19)}$	$2.3_{(5)}$	$34.5_{(13)}$	$0.6_{(3)}$	-	$47.7_{(12)}$	100.0	$0.19_{(3)}$	$0.03_{(1)}$	$0.79_{(2)}$	$0.01_{(1)}$	$0.99_{(1)}$	$2.01_{(1)}$	0.19
E-00	Fms	-	12.0	1.4	35.8	1.3	-	49.5	100.0	0.15	0.02	0.80	0.02	1.01	1.99	0.15
		-	13.7	2.0	33.3	2.1	-	48.9	100.0	0.17	0.02	0.75	0.03	1.01	1.99	0.18
		-	14.7	2.0	32.7	2.1	-	48.5	100.0	0.19	0.02	0.74	0.03	1.00	2.00	0.19
		-	15.7	2.3	32.3	2.0	-	47.6	100.0	0.20	0.03	0.74	0.03	1.00	2.00	0.20
		-	16.0	2.3	32.2	2.0	-	47.5	100.0	0.21	0.03	0.74	0.03	1.00	2.00	0.20
		-	17.4	2.4	30.6	1.0	-	48.7	100.0	0.22	0.03	0.70	0.02	1.02	1.98	0.23
	Mean	-	$14.9_{(19)}$	$2.1_{(4)}$	$32.8_{(17)}$	$1.8_{(5)}$	-	$48.5_{(8)}$	100.0	$0.19_{(3)}$	$0.03_{(0)}$	$0.75_{(3)}$	$0.03_{(1)}$	$1.00_{(1)}$	$2.00_{(0)}$	0.19
E-01	$L_{carb-sil}$	4.9	12.6	0.9	29.8	2.4	0.8	48.6	100.0	-	-	-	-	-	-	0.18
		5.7	13.8	1.0	26.9	1.1	1.5	50.0	100.0	-	-	-	-	-	-	0.21
		6.3	13.7	1.1	28.7	1.6	1.2	47.4	100.0	-	-	-	-	-	-	0.20
		7.3	14.9	1.1	28.4	1.7	1.2	45.4	100.0	-	-	-	-	-	-	0.22
		7.5	13.5	0.9	29.6	1.2	0.8	46.5	100.0	-	-	-	-	-	-	0.20
	Mean	$6.3_{(9)}$	$13.7_{(8)}$	$1.0_{(1)}$	$28.7_{(9)}$	$1.6_{(5)}$	$1.1_{(2)}$	$47_{(2)}$	100.0	-	-	-	-	-	-	0.20
	Fms	-	5.4	0.9	39.2	3.5	-	51.0	100.0	0.07	0.01	0.85	0.05	1.01	1.99	0.07
		-	5.5	1.0	38.6	3.4	-	51.4	100.0	0.07	0.01	0.84	0.05	1.02	1.98	0.07
		-	4.8	0.8	39.1	3.5	-	51.8	100.0	0.06	0.01	0.85	0.05	1.02	1.98	0.06
		-	7.4	1.3	38.4	3.4	-	49.5	100.0	0.09	0.02	0.85	0.05	1.00	2.00	0.09
		-	4.6	0.7	39.6	3.6	-	51.6	100.0	0.05	0.01	0.86	0.05	1.01	1.99	0.06
	Mean	-	$5.5_{(9)}$	$1.0_{(2)}$	$39.0_{(5)}$	$3.5_{(1)}$	-	$51.1_{(9)}$	100.0	$0.07_{(1)}$	$0.01_{(0)}$	$0.85_{(1)}$	$0.05_{(0)}$	$1.01_{(1)}$	1.99	0.07

Fms—ferromagnesite, $L_{carb-sil}$—carbonate-silicate melt; number of cations p.f.u. was calculated per 3 oxygen atoms; *—calculated after the sum deficit; Mean—averaged compositions based on 30 analyses, the values in parentheses are one sigma errors of the means based on replicate electron microprobe analyses reported as least units cited; $3.3_{(9)}$ should be read as 3.3 ± 0.9 wt.%, and $14.9_{(19)}$ should be read as 14.9 ± 1.9 wt.%; Fe#—Fe number—Fe/(Fe + Mn + Mg + Ca), mol.

The only silicate phase crystallized as a result of interaction in the olivine–siderite–sulfur system at 1150 °C (60 h) is newly formed orthopyroxene. Representative micrographs of orthopyroxene crystals in the sample are shown in Figure 2a,g,h, and their Raman spectra are shown in Figure 5a,b. Most orthopyroxene crystals are characterized by a uniform composition corresponding to $enstatite_{(78)}$–$ferrosilite_{(22)}$ with a formula $Fe_{0.43}Mn_{0.04}Mg_{1.52}Ca_{0.01}Si_2O_6$ (Figure 4, Table 7). However, about 20% of the crystals exhibits complex zoning (Figure 6a–c) of three or four zones. For example, the Fe number (molar ratio Fe/(Fe + Mg + Ca + Mn)) of alternating zones (from the edge to the center) can vary in a row 0.23 → 0.31 → 0.17 → 0.42 (Figure 6a–c). Some orthopyroxene crystals contain pyrrhotite inclusions. Recrystallized olivine in the sample occurs as single crystals up to 20 μm in size and has a composition of $Fe_{0.12}Mn_{0.01}Mg_{1.85}SiO_4$ (Table 7).

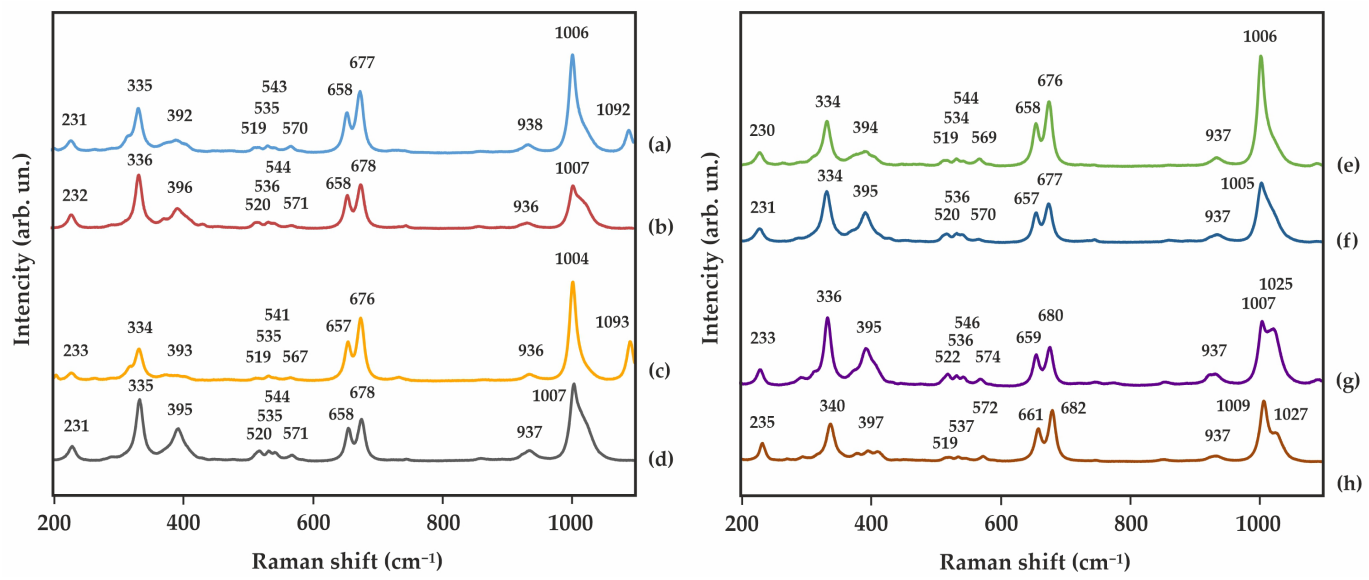


Figure 5. Representative Raman spectra of newly formed orthopyroxene: (**a**,**b**) run E-76, 1150 °C; (**c**,**d**) run E-97, 1250 °C; (**e**,**f**) run E-00, 1350 °C; (**g**,**h**) run E-01, 1450 °C; arb. un.—arbitrary unit.

At a higher temperature (1250 °C) and run duration of 40 h, interactions in the olivine–siderite–sulfur system result in the formation of an association of newly formed orthopyroxene, pyrrhotite, and ferromagnesite. All the initial phases are completely consumed during experiments. The general structure of the sample is shown in Figure 1b.

On the base of sample textures examining, we have distinguished three main types of polycrystalline aggregates in the sample. The first type is presented by aggregates of orthopyroxene and pyrrhotite, with a general shape of the sections of larger faceted crystals with a rhomboprismatic habit (Figures 1b and 6d,e). We interpreted these aggregates as ones replacing starting Fe,Ni-bearing forsterite crystals and thus inheriting their shape. The second type of polycrystalline aggregates consist of pyrrhotite and ferromagnesite, often characterized by a hexagonal shape (Figures 1b and 6e). We supposed these aggregates replaced starting siderite and inherited faceting of hexagonal cross-sections of siderite crystals.

In addition, the sample contains third type of zonal aggregates, the outer zone of which is represented by orthopyroxene or a polycrystalline aggregate of orthopyroxene + pyrrhotite, and the inner zone by ferromagnesite (Figures 1b and 6g). Compositions of the newly formed phases within the sample are quite homogeneous, regardless of the polycrystalline aggregates in which they are present. The orthopyroxene composition corresponds to $Fe_{0.45}Mn_{0.05}Mg_{1.49}Ca_{0.01}Si_2O_6$ (Table 7, Figure 4), and the ferromagnesite composition varies from $Fe_{0.14}Mn_{0.02}Mg_{0.81}Ca_{0.02}CO_3$ to $Fe_{0.25}Mn_{0.02}Mg_{0.75}CO_3$ (Table 6, Figure 4). Pyrrhotite is characterized by an admixture of Ni (0.5–0.7 wt.%), and its formula corresponds to $Fe_{0.87}Ni_{0.1}S$ (Table 3).

At a temperature of 1350 °C (20 h), the interaction of olivine and siderite with sulfur leads to the crystallization of orthopyroxene and ferromagnesite, as well as to the formation of a sulfide melt (Figures 7a and 8a–c). Morphological criteria to distinguish solid pyrrhotite from quenched sulfide melt are as follows. Solid pyrrhotite, crystallized in the runs at 1150–1250 °C, is presented by euhedral crystals or polycrystalline aggregates with linear boundaries between inner grains, and quenched sulfide melt is presented by homogeneous droplets or spheres with no inner grain boundaries (Figure 6h,i). In addition, it is worth noting, that the melting temperature of pyrrhotite in multicomponent carbonate-silicate–sulfide systems is about 1300 °C at 6.3 GPa [19,20]. The sample predominantly consists of polycrystalline zoned aggregates (averaging 200–500 μm in size),

with ferromagnesite in the central parts and orthopyroxene ± sulfide melt in the outer parts (Figure 6h,i, Figures 7a and 8a,b). Small sulfide droplets often outline the outer boundaries of these zoned aggregates. The interstitions between the zoned aggregates are filled with ferromagnesite and droplets of quenched sulfide melt, varying in size from 20 to 300 μm. The composition of the obtained orthopyroxene corresponds to the formula $Fe_{0.40–0.55}Mn_{0.04–0.06}Mg_{1.37–1.53}Ca_{0.02–0.03}Si_2O_6$ (Table 7, Figure 4), and that of ferromagnesite is $Fe_{0.15–0.22}Mn_{0.02–0.03}Mg_{0.70–0.80}CO_3$ (Table 6). The sulfide melt is characterized by the atomic ratio Fe:Ni:S = 47.2:0.5:52.3 (Table 4).

Table 7. Compositions of silicate phases after experiments in olivine–siderite–sulfur system.

Run N	Phase	Mass Concentrations, wt.%							Cations per Formula Unit, p.f.u.						
		SiO_2	FeO	MnO	MgO	CaO	NiO	Total	Si	Fe	Mn	Mg	Ca	Ni	Total
E-76	Opx	57.4	8.7	0.9	32.2	-	0.4	99.6	2.01	0.26	0.03	1.68	-	0.01	3.99
		56.0	12.8	1.6	29.1	-	-	99.5	2.01	0.39	0.05	1.55	-	-	3.99
		56.0	13.5	1.0	28.8	0.1	0.3	99.8	2.01	0.41	0.03	1.54	0.01	0.01	3.99
		55.8	14.7	1.2	28.0	-	-	99.6	2.01	0.44	0.04	1.51	-	-	3.99
		55.3	15.5	1.6	27.0	-	-	99.4	2.01	0.47	0.05	1.46	-	-	3.99
		54.7	16.7	1.6	26.5	0.1	-	99.5	2.00	0.51	0.05	1.44	0.01	-	4.00
		54.3	17.0	1.7	26.2	0.3	-	99.4	1.97	0.52	0.05	1.42	0.01	-	3.99
		54.5	18.0	1.7	25.3	-	-	99.6	2.00	0.55	0.05	1.39	-	-	4.00
	Mean	$55.5_{(8)}$	$14.3_{(22)}$	$1.4_{(3)}$	$28.2_{(17)}$	$0.1_{(1)}$	$0.1_{(1)}$	99.6	$2.00_{(1)}$	$0.43_{(7)}$	$0.04_{(1)}$	$1.52_{(7)}$	$0.01_{(1)}$	-	4.00
	Ol[s]	41.7	6.4	0.5	51.3	-	-	99.9	1.01	0.13	0.01	1.85	-	-	2.99
		41.2	5.7	0.6	51.7	0.2	-	99.3	1.00	0.12	0.01	1.87	0.01	-	3.00
	Mean	$41.6_{(2)}$	$6.1_{(2)}$	$0.5_{(1)}$	$51.4_{(3)}$	$0.1_{(1)}$	-	99.7	$1.01_{(0)}$	$0.12_{(0)}$	$0.01_{(0)}$	$1.85_{(1)}$	-	-	2.99
E-97	Opx	56.3	12.6	1.3	29.5	-	-	99.7	2.01	0.38	0.04	1.57	-	-	3.99
		55.6	13.2	1.7	28.7	0.1	-	99.3	2.00	0.40	0.05	1.54	0.01	-	4.00
		55.6	14.8	1.8	27.7	-	-	99.9	2.01	0.45	0.06	1.49	-	-	4.00
		55.2	15.9	1.9	26.7	0.2	-	99.9	2.00	0.48	0.06	1.44	0.01	-	4.00
		54.8	16.9	2.3	25.9	-	-	100.0	2.00	0.52	0.07	1.41	-	-	4.00
	Mean	$55.4_{(4)}$	$14.8_{(9)}$	$1.7_{(2)}$	$27.6_{(7)}$	$0.1_{(1)}$	-	99.6	$2.00_{(1)}$	$0.45_{(3)}$	$0.05_{(1)}$	$1.49_{(3)}$	$0.01_{(0)}$	-	4.00
E-00	Opx	55.9	13.4	1.3	28.5	0.4	-	99.4	2.01	0.40	0.04	1.53	0.02	-	3.99
		55.2	14.9	1.5	27.1	0.8	-	99.5	2.00	0.45	0.05	1.47	0.03	-	4.00
		54.9	15.4	1.6	27.2	0.4	-	99.5	2.00	0.47	0.05	1.47	0.02	-	4.00
		54.8	16.8	1.9	25.7	0.4	-	99.5	2.01	0.51	0.06	1.40	0.02	-	4.00
		54.6	17.9	1.9	25.1	0.4	-	99.8	2.00	0.55	0.06	1.37	0.02	-	4.00
	Mean	$55.0_{(3)}$	$15.8_{(11)}$	$1.7_{(2)}$	$26.7_{(8)}$	$0.4_{(3)}$	-	99.5	$2.00_{(0)}$	$0.48_{(4)}$	$0.05_{(1)}$	$1.45_{(4)}$	$0.02_{(1)}$	-	4.00
E-01	Opx[1]	58.7	3.6	0.6	35.7	1.2	-	99.8	2.01	0.10	0.02	1.82	0.05	-	3.99
		58.0	5.3	0.6	34.8	1.0	-	99.8	2.00	0.15	0.02	1.79	0.04	-	4.00
		57.9	6.6	0.8	33.9	0.7	-	99.8	2.01	0.19	0.02	1.75	0.02	-	3.99
		57.1	7.9	0.8	32.6	1.0	-	99.4	2.00	0.23	0.02	1.71	0.04	-	4.00
		56.1	8.4	0.9	33.0	1.0	-	99.4	1.98	0.25	0.03	1.73	0.04	-	4.02
	Mean	$57.6_{(7)}$	$6.6_{(14)}$	$0.5_{(3)}$	$34.2_{(11)}$	$0.8_{(5)}$	-	99.6	$2.00_{(1)}$	$0.19_{(4)}$	$0.02_{(1)}$	$1.77_{(4)}$	$0.03_{(2)}$	-	4.00
	Opx[2]	56.5	10.1	1.0	31.2	0.8	-	99.7	2.00	0.30	0.03	1.65	0.03	-	4.00
		56.1	11.6	1.4	30.2	0.3	-	99.7	2.00	0.35	0.04	1.61	0.01	-	4.00
		56.0	12.2	1.0	29.9	0.2	-	99.4	2.00	0.37	0.03	1.59	0.01	-	4.00
		55.6	13.2	1.0	29.6	0.2	0.3	99.8	1.99	0.39	0.03	1.58	0.01	0.01	4.01
	Mean	$56.1_{(5)}$	$11_{(1)}$	$1.0_{(2)}$	$31_{(1)}$	$0.4_{(3)}$	-	99.6	$1.99_{(2)}$	$0.33_{(3)}$	$0.03_{(1)}$	$1.64_{(5)}$	$0.02_{(1)}$	-	4.01

Opx—orthopyroxene, Opx[1]—orthopyroxene (group 1 on composition), Opx[2]—orthopyroxene (group 2 on composition), Ol—olivine, [s]—single grains; number of cations p,f,u, was calculated per 6 oxygen atoms for pyroxenes and per 4 oxygen atoms for olivines; Mean—averaged compositions based on 28 analyses, the values in parentheses are one sigma errors of the means based on replicate electron microprobe analyses reported as least units cited; $1.7_{(2)}$ should be read as 1.7 ± 0.2 wt.%, and $15.8_{(11)}$ should be read as 15.8 ± 1.1 wt.%.

It was experimentally demonstrated that at the highest temperature (1450 °C, 20 h), crystallization of an association of newly formed orthopyroxene and ferromagnesite, as well as the generation of two immiscible melts, carbonate–silicate and sulfide (Figures 7b

and 8d–f), occur. The upper part of the sample contains a quenched carbonate–silicate melt, represented by microdendrites of Ca,Mg,Fe–carbonates, pyroxenes and olivine, in which large droplets of quenched sulfide melt, as well as large crystals of orthopyroxene are located (Figure 8f). The lower part of the sample (about 2/3 of the total reaction volume) is represented by a carbonate–silicate matrix, in which droplets of quenched sulfide melt are located (Figure 7b).

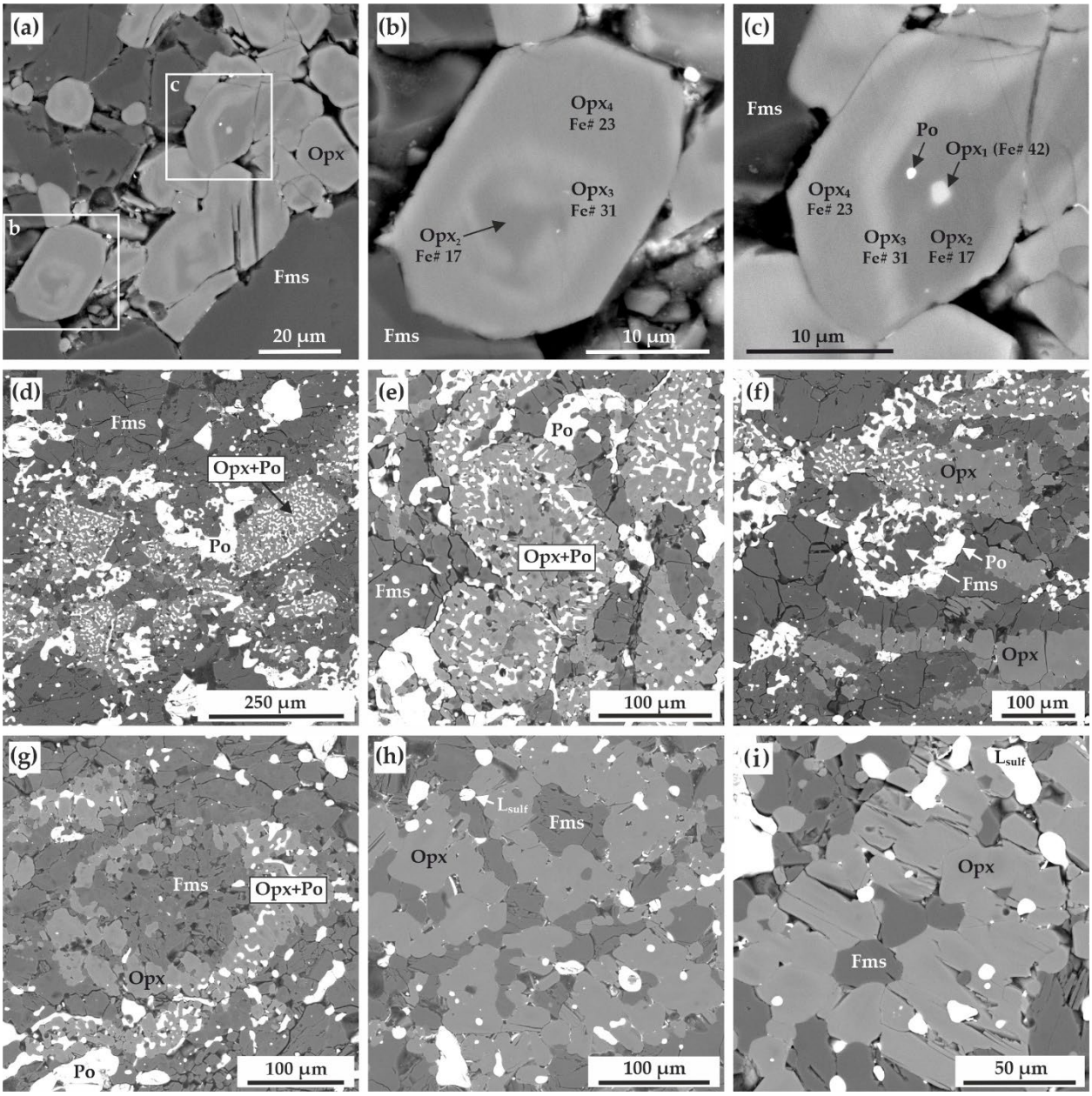


Figure 6. SEM micrographs (BSE regime) of polished sections of the samples, after experiments in olivine–siderite–sulfur at 1150 °C and 60 h (**a**–**c**), 1250 °C and 40 h (**d**–**g**), 1350 °C and 20 h (**h**,**i**): (**a**) zoned orthopyroxene crystals surrounded by ferromagnesite; (**b**,**c**) enlarged fragments of (**a**), illustrating zoned structure orthopyroxene crystals and pyrrhotite inclusions therein; (**d**,**e**) polycrystalline aggregates of orthopyroxene and pyrrhotite, inheriting crystal shapes of the initial olivine; (**f**) polycrystalline aggregate of ferromagnesite and pyrrhotite, inheriting crystal shapes of the initial siderite; (**g**–**i**) zonal aggregate, with the outer zone represented by orthopyroxene or a polycrystalline aggregate of orthopyroxene + pyrrhotite, and the inner zone consisted of ferromagnesite. Opx—orthopyroxene, Fms—ferromagnesite, Po—pyrrhotite, L_{sulf}—sulfide melt, Fe#—Fe number—Fe/(Fe + Mg + Ca + Mn), molar.

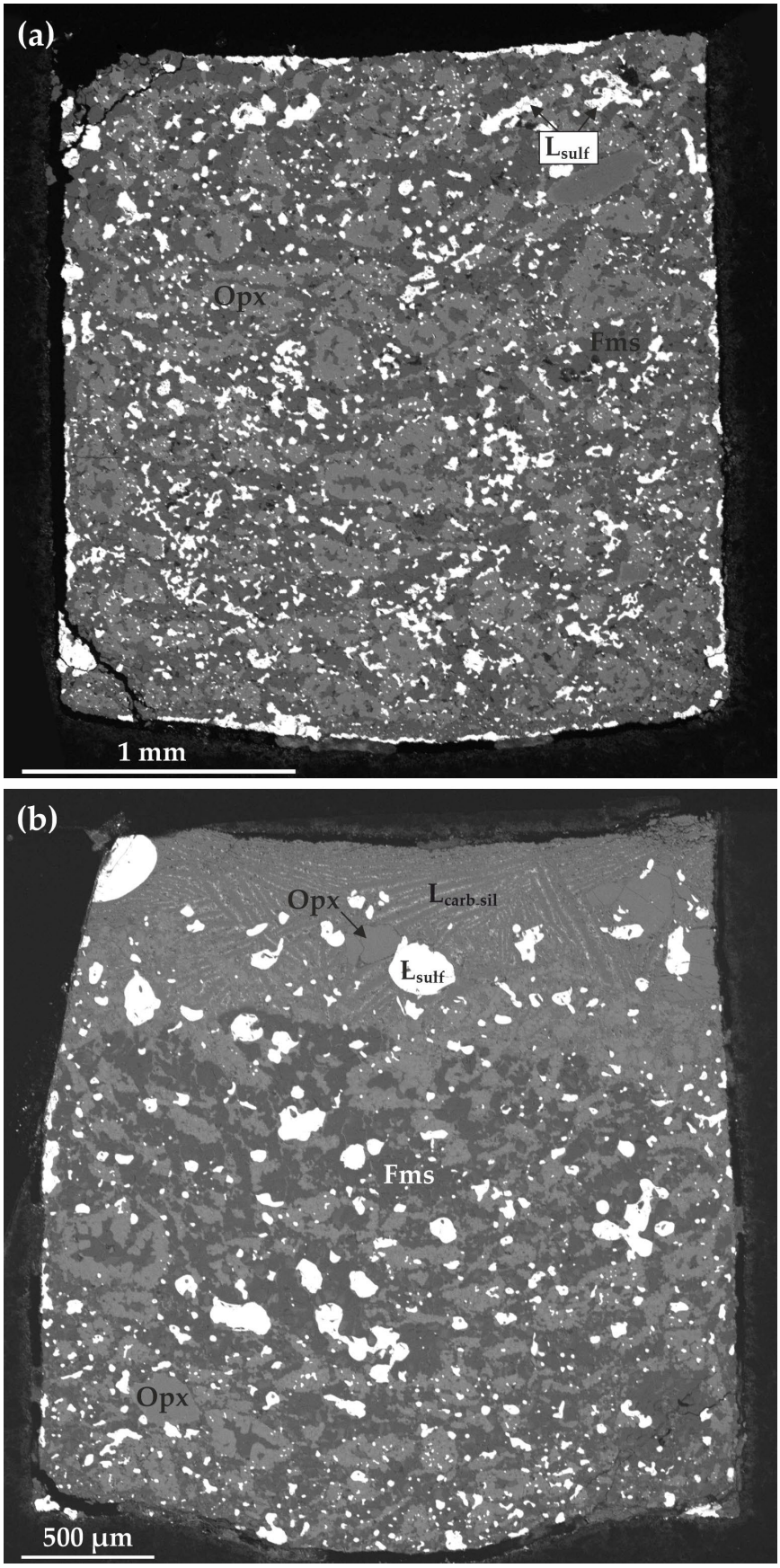


Figure 7. SEM micrographs (BSE regime) of polished vertical sections of the samples: (**a**) run E-00, 1350 °C; (**b**) run E-01, 1450 °C; Opx—orthopyroxene, Fms—ferromagnesite, $L_{carb-sil}$—carbonate-silicate melt, L_{sulf}—sulfide melt.

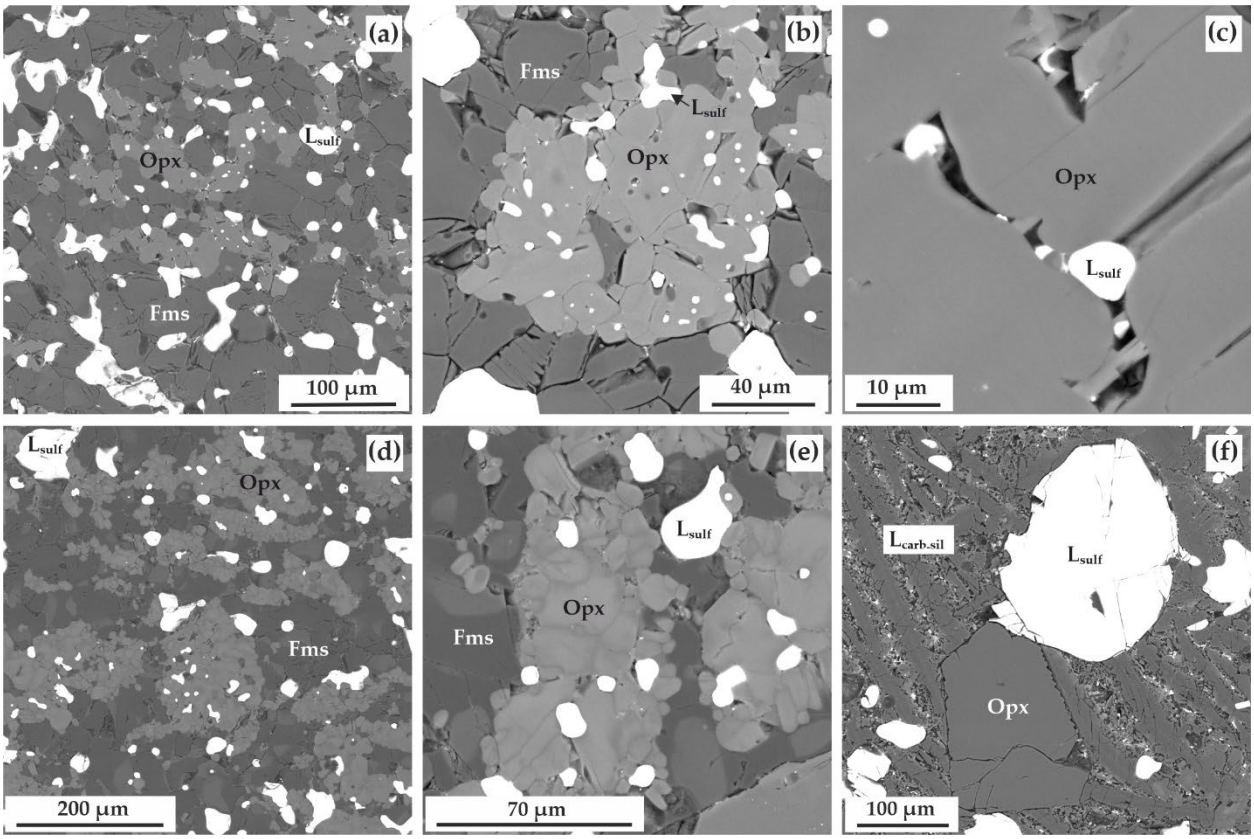


Figure 8. SEM micrographs (BSE regime) of polished sections of the samples, after experiments in olivine–siderite–sulfur at 1350 °C and 20 h (**a**–**c**), 1450 °C and 20 h (**d**–**f**): (**a**,**b**) polycrystalline aggregates of orthopyroxene and ferromagnesite, coexisting with sulfide melt droplets; (**c**) sulfide melt droplets in the interstitions between orthopyroxene crystals; (**d**,**e**) polycrystalline aggregates of orthopyroxene and ferromagnesite, coexisting with sulfide melt droplets; (**f**) microdendritic aggregate of the quenched carbonate-silicate melt, containing sulfide melt droplets as well as large orthopyroxene crystals. Opx—orthopyroxene, Fms—ferromagnesite, L_{sulf}—sulfide melt, $L_{carb-sil}$—carbonate–silicate melt.

Newly formed orthopyroxene in this matrix forms specific unevenly spotted polycrystalline aggregates (Figure 8d,e), in which two orthopyroxenes of different composition are distinguished: $Mg_{1.77}Fe_{0.19}Mn_{0.02}Ca_{0.03}Si_2O_6$ and $Mg_{1.64}Fe_{0.33}Mn_{0.03}Ca_{0.03}Si_2O_6$ (Table 7). Several large orthopyroxene crystals were also found in the carbonate–silicate matrix of the samples, characterized by a similar type of zoning (Figure 9a–c) and containing inclusions of sulfide melt (Figure 9b). In ferromagnesite, as in orthopyroxene, two varieties (two trends) are distinguished by composition, while zoned aggregates for carbonate phases were not established. The average composition of ferromagnesite corresponds to the formula $Mg_{0.87}Fe_{0.06}Mn_{0.01}Ca_{0.06}CO_3$ (Table 6, Figure 4). Sulfide melt, both forming rounded segregations in the sample and occurring as inclusions in orthopyroxene, is characterized by an atomic ratio of Fe:Ni:S = 46.8:0.5:52.7 (Table 4). Carbonate–silicate melt contains ~6.3 wt.% SiO_2, ~13.7 wt.% FeO, and ~1.1 wt.% SO_3 (Table 6). It should be noted that by the composition of carbonate–silicate melt, we mean averaged broad-beam analyses of quenched micro-dendritic aggregates.

Summarizing this section, we would like to stress that reported assemblages can be interpreted as near-equilibrium. In the experimental samples, phase assemblage of orthopyroxene + pyrrhotite/sulfide melt + ferromagnesite was formed. At 1150 °C, magnetite was crystallized, and at 1450 °C, carbonate–silicate melt was generated. Compositions of

most phases are quite close to ones calculated based on mass balance and stoichiometry of chemical reactions.

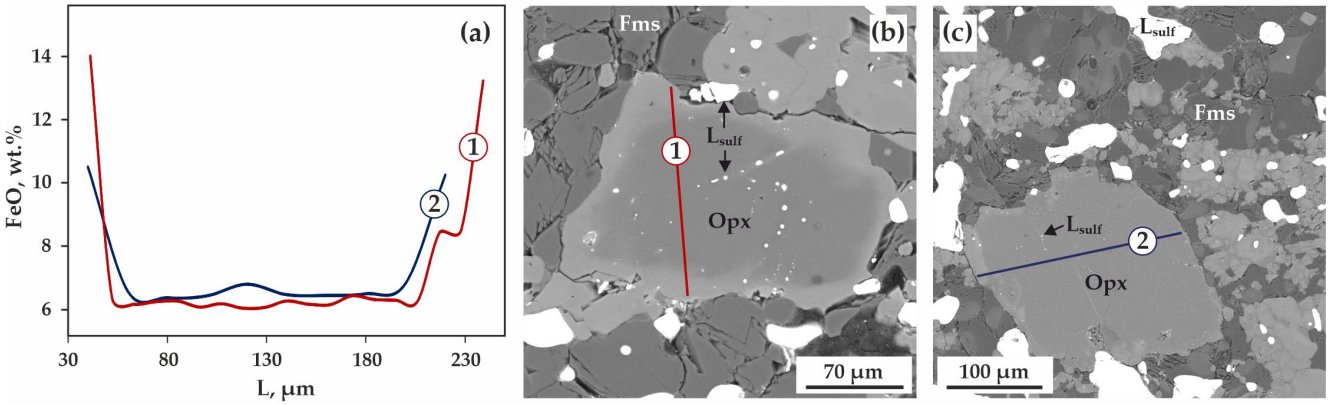


Figure 9. Representative compositional profiles ((1) and (2)) of the FeO distribution in orthopyroxene, newly-formed in olivine–siderite–sulfur system, as well as (**a**) SEM micrographs (BSE regime) of polished sections of the samples, illustrating orthopyroxene crystals with corresponding lines of profiles recorded ((**b**) 1350 °C and (**c**) 1450 °C).

3.2. Carbon Phases in the Olivine–Siderite–Sulfur System

A detailed study of the micromorphology of diamond seed crystals (Figure 10) reveals that they were partially dissolved during experiments. The degree of dissolution of the diamond seeds was quantified by weighting seed crystals before and after experiments. The weight loss was in a range of 6–14 wt.%, with no consistent pattern or any dependence with temperature and duration. The weight loss varied both between the seeds from the same run, and between the seeds from different runs. We assume that diamond dissolution occurred in intergranular fluid or carbonate–silicate melt during the experiments. Graphite is completely absent from the samples obtained in all experiments, and there are no signs of recrystallization of graphite in the capsules at a contact with the samples. At 1150–1350 °C, the octahedral faces of the diamond seed crystals are covered with numerous inversely oriented triangular etch pits (Figure 10a,b,d,e,g,h), which are traditionally referred to as negative trigons [35]. On the {111} faces, negative trigons of two types are distinguished: pyramidal with relatively flat walls and flat-bottomed, characterized by steeper walls (Figure 10a,b,d,e). The sizes of most of these triangular etch pits are 35–40 μm (1150 °C) and 20–90 μm (1250–1350 °C). Layer-by-layer dissolution on the octahedron faces is poorly developed; the formation of jagged structures is established along the edges between the {111} faces (Figure 10a,b,d,h). The cube faces are completely covered with numerous etch pits—rectangular flat-bottomed, square flat-bottomed, or square pyramidal—with sides parallel to the crystal edges (Figure 10c,f,i). The sizes of these pits are 10–25 μm (1150 °C) and 30–50 μm (1250–1350 °C) on average. At the highest temperature of 1450 °C, under conditions when two melts, carbonate–silicate and sulfide, are formed in the system, hexagonal etch pits are established on the octahedron faces of diamond seed crystals (Figure 10j,k). These pits are flat-bottomed, characterized by both gently sloping and steep walls; the average pit size is 50–60 μm up to 180 μm on some faces (Figure 10j). The {100} faces of the diamond seed crystals are almost completely covered with numerous small square and rectangular etch pits, 5–10 μm in size. In addition, unusual positive relief elements, rounded areas with a relatively smooth surface, are established on the cube faces (Figure 10l). We suppose that they occurred at the contact between the initial cube faces of seed crystals and droplets of sulfide melt, which protected the diamond surface from dissolution, and thus, after the dissolution of the remaining facet surface, positive relief features were formed.

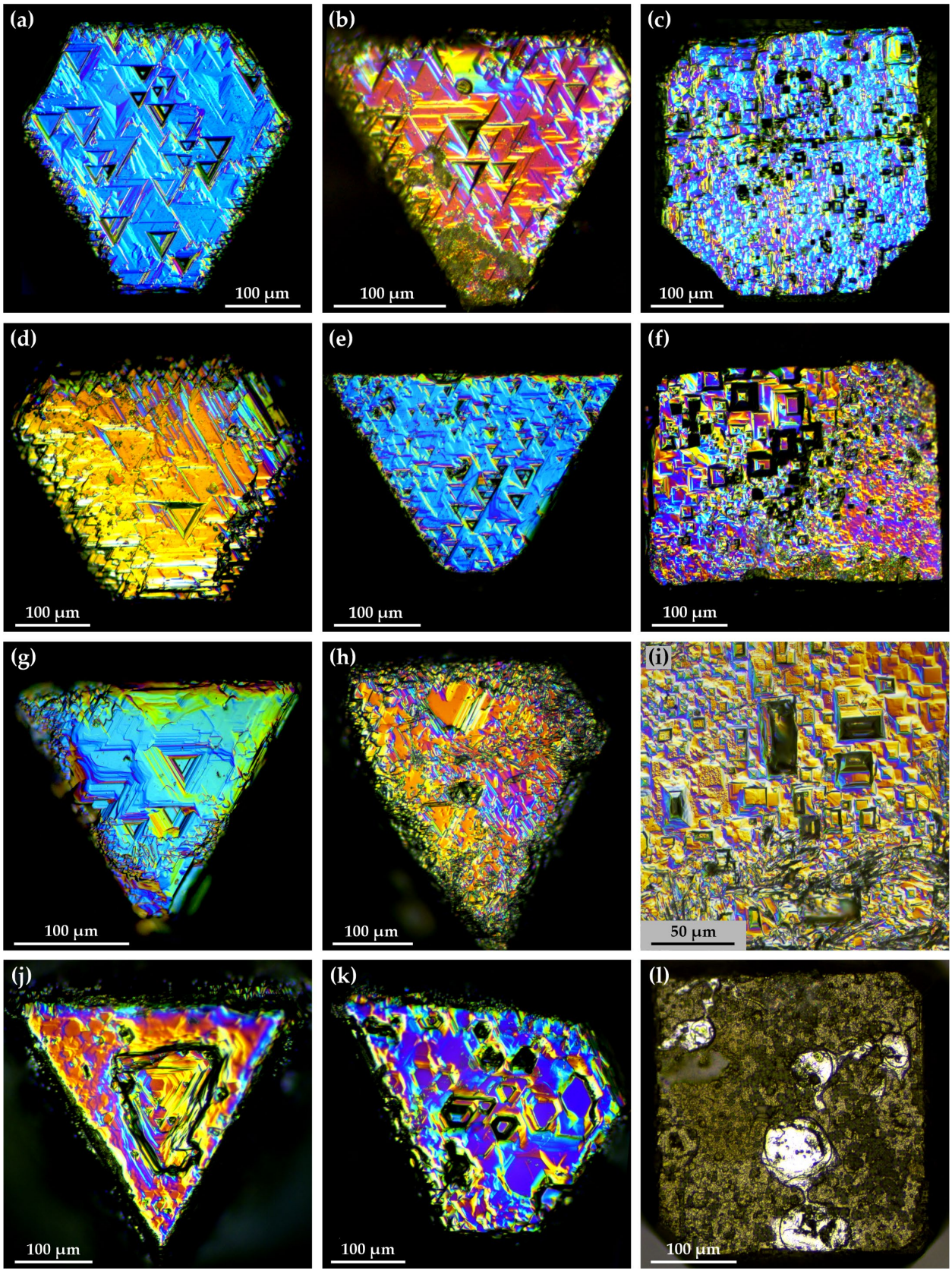


Figure 10. DIC-micrographs of diamond seed crystals with dissolution patterns: (**a**–**c**) run E-76, 1150 °C; (**d**–**f**) run E-97, 1250 °C; (**g**–**i**) run E-00, 1350 °C; (**j**–**l**) run E-01, 1450 °C.

4. Discussion

4.1. Reconstruction of Interaction Processes in the Olivine–Siderite–Sulfur System

A detailed study of the phase relationships and chemical compositions of the final phases, as well as a comparison of the obtained results with the available literature data, allowed us to reconstruct the interaction processes in the olivine–siderite–sulfur system at 6.3 GPa and in the range of 1150–1450 °C. It was experimentally established that over the entire temperature range, the starting phases were completely consumed as a result of a complex of sulfidation reactions of Fe,Ni–olivine and siderite, carbonate + silicate ± oxide exchange reactions, siderite redox-dissociation, and partial melting processes.

At the P,T-parameters of the experiments, sulfur is present in the form of a melt (or, given its very high volatility, in the form of a melt/fluid) [36], and therefore Fe,Ni–olivine, siderite, and sulfur melt can be considered as the starting phase association entering into the reactions. We have previously demonstrated that the interaction of Fe,Ni–olivine (completely identical to one used in the present study) with sulfur melt at 6.3 GPa and 1150–1450 °C is accompanied by the recrystallization of olivine in sulfur melt, the extraction of Fe and Ni from olivine into the melt, and the subsequent formation of sulfides and low- or iron-free orthopyroxene [37] according to the sulfidation reaction:

$$2(Mg,Fe,Ni)_2SiO_4 + 2S^0{}_{liq} \rightarrow 2(Fe,Ni)S + 2MgSiO_3 + O_2. \quad (1)$$

We have to stress that in the reaction (1) and all further reactions silicates, oxides, and sulfides are directly observed phases, while O_2 and other oxidized fluids are inferred products. Moreover, the crystallization of newly formed orthopyroxene by this reaction is due to the fact that the extraction of Fe and Ni from olivine leads to an excess of SiO_2 relative to MgO, i.e., to a molar ratio of SiO_2/MgO of ~1, corresponding to orthopyroxene, instead of the $SiO_2/MgO = 0.5$ characteristic of olivine.

It has been experimentally demonstrated that the interaction of siderite ((Fe,Mg,Mn,Ca)CO_3) with sulfur melt also leads to its recrystallization, iron extraction into melt, and sulfide formation (or the generation of sulfide melt). However, given that the ongoing extraction of iron from siderite into sulfide disrupts the stoichiometric balance of divalent cations and carbonate ions within its composition, the crystallization of newly formed ferromagnesite requires the addition of divalent cations from silicates. The most probable overall reaction of interaction in the system at 1150–1250 °C can be shown as follows:

$$\begin{aligned}(Fe, Mg, Mn)CO_3 + 2(Mg, Fe, Ni)_2 SiO_4 + 2Si_{kq} \rightarrow \\ \rightarrow (Mg, Fe, Mn, Ca)CO_3 + 2(Fe, Ni)S + 2(Mg, Fe)SiO_3 + O_2.\end{aligned} \quad (2)$$

The formation of complex iron zoning in orthopyroxene crystals may be due to the predominant contribution of reaction (1) and reaction (2) to its crystallization at different stages of the experiment: the olivine sulfidation reaction produces low-iron orthopyroxene, while the general sulfidation reaction of siderite and olivine produces high-iron orthopyroxene.

Reaction (2) does not address the very interesting fact of magnetite formation as numerous inclusions in ferromagnesite at 1150 °C, which deserves further consideration. It is now known that at depths of about 200 km, at temperatures above 1100 °C and oxygen fugacity (fO_2) values below the CCO (C–CO) buffer but above the WM (wüstite–magnetite) buffer, siderite undergoes redox dissociation, resulting in the formation of magnetite, elemental carbon, and O_2/CO_2 fluid [38,39] (Figure 10a,b):

$$3FeCO_3 \rightarrow Fe_3O_4 + 3C^0 + 2.5O_2 \text{ fluid}. \quad (3)$$

In reaction (3), only the magnetite phase is directly observed, while elemental carbon and O_2 are inferred products. Since the starting siderite contained impurities of MgO, MnO, and CaO, its redox dissociation reaction (3) occurred partially, resulting in the formation of ferromagnesite crystals with magnetite inclusions in place of some of the starting siderite crystals. Moreover, the detection of SiO_2 impurities in magnetite inclusions in concentrations described for natural magnetites from mantle xenoliths [40–42] indicates the participation of silicate phases in its formation, during the combined implementation of reactions (2) and (3).

Further (or parallel) interaction of the resulting magnetite with sulfur melt leads to sulfidation of the magnetite [43]:

$$Fe_3O_4 + 5S^0 = 3FeS + 2SO_2, \quad (4)$$

this is evidenced by the formation of two-phase inclusions of magnetite and pyrrhotite in ferromagnesite.

At temperatures of 1350–1450 °C, in addition to the processes described above, partial melting occurs in the system, forming a sulfide melt (1350 °C) or two immiscible melts: carbonate–silicate and sulfide (1450 °C). Melting temperature of $FeCO_3$ at 6.0 GPa is 1580 °C [44]. It was established that under these conditions, recrystallization of newly formed orthopyroxene in the melt occurred, leading to an increase in crystal size, as well as a change in its chemical composition, most clearly manifested in an increase in FeO content. Evidence of this process is the unevenly spotted structure of orthopyroxene crystal aggregates (Figure 8e), as well as single large orthopyroxene crystals with zoning (Figure 9a,c).

After presenting the detailed reconstruction of the interaction processes, but before the discussion of diamond dissolution, we would like to discuss redox conditions in the experiments. Unfortunately, since we can not definitely say what exact phase assemblage, phase compositions and phase proportions presented in the reaction volume at an intermediate stages of the experiments, we can only approximately estimate oxygen fugacities in the samples. As mentioned above, in carbonate-bearing systems, graphite capsules buffer the whole charge near CCO buffer. To our knowledge, there is no data on the position of elemental sulfur/sulfide ($S^0 \rightarrow S^{2-}$) buffer in the T-fO_2 space. However, V. Matjushkin and co-authors (2016) [45] demonstrated that at high pressures, sulfate-to-sulfide transition ("SST", $S^{6+} \rightarrow S^{2-}$) buffer is located near the fayalite–magnetite–quartz (FMQ) buffer. We suppose that elemental sulfur-to-sulfide buffer has to be located below SST buffer, under more reduced conditions. Figure 11 shows that reaction curve of siderite redox-dissociation and magnetite formation is located just below CCO buffer. Given the fact that dissolution of diamond took place, we can conclude that all the processes caused net sample oxidation. Thus, we have roughly estimated redox conditions in the samples to be near CCO buffer, but slightly above it to enable diamond dissolution conditions (fO_2 ~ CCO + 0.5 log. units).

The issue of diamond dissolution during the interaction of Fe,Ni–olivine and siderite with sulfur melt deserves special attention. It is currently known that in multicomponent S- or sulfide-containing systems [31,46–49], an increase in the bulk concentrations of S inhibits diamond formation. Silicate matter also has an inhibitory effect on diamond growth [50]. In the work of I.D. Novoselov and co-authors (2026) [51], it is established that in silicate–carbonate–sulfide environments with a bulk sulfur concentration of 3 wt.%, even when saturated with carbon, diamond crystallization does not occur, but, on the contrary, its dissolution is observed. This may be due to the fact that sulfide and sulfur-rich carbonate–silicate melts formed in silicate–carbonate–sulfide systems are characterized by low capacity for both carbon dissolution and carbon transport. In addition to the potential inhibitory effect of sulfur and silicates on diamond formation in the olivine–

siderite–sulfur system, should also be discussed. Below we present our hypothesis on a probable mechanism of diamond dissolution, since we did not study the fluid composition in situ and can operate only inferred fluid compositions according to reaction schemes (1)–(4). We suppose that implementation of all sulfidation reactions as well as siderite redox-dissolution reaction might produce oxidized fluid, consisting of O_2, CO_2, and SO_2. Probably, in a temperature range of 1150–1350 °C, O_2, CO_2, and SO_2 presented as components of segregated intergranular fluid, and at higher temperature they were dissolved in a carbonate–silicate melt. Interaction of this oxidized fluid/melt with dissolved fluid with diamond seed crystals results in diamond dissolution.

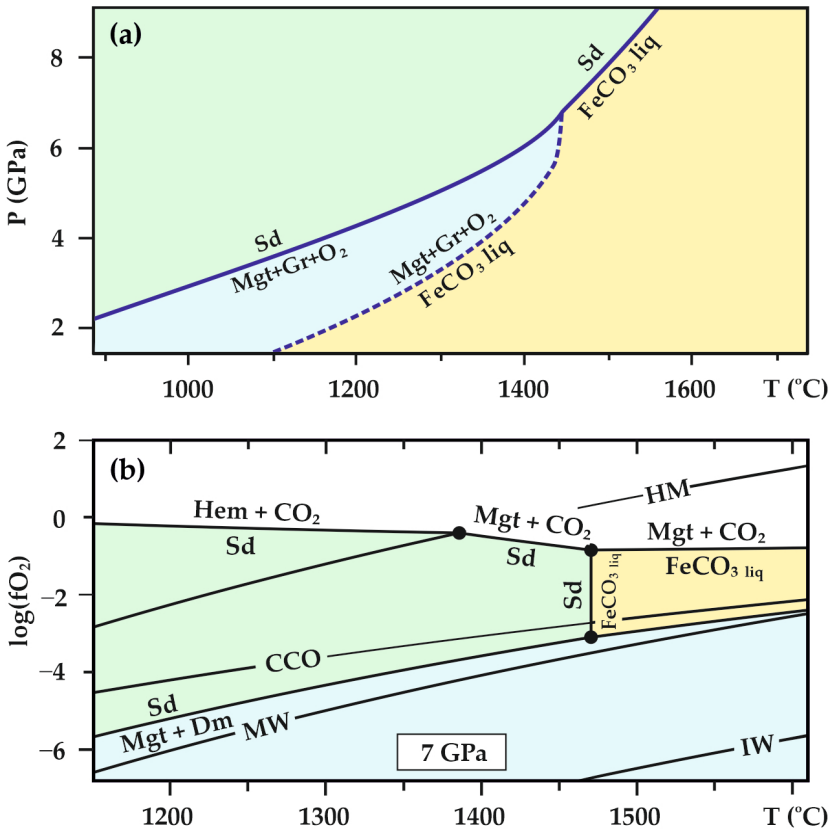


Figure 11. Experimentally determined melting and redox dissociation parameters of siderite [38,39]; (**a**) and the T-fO_2 diagram of the Fe–C–O_2 system [38]; in an isobaric section (7 GPa), displaying the stability fields of siderite and $FeCO_3$ melt and their intersections with the CCO, hematite–magnetite (HM) and magnetite–wüstite (MW) buffers (**b**). Hem—hematite, Sd—siderite, Mgt—magnetite, Gr—graphite, Dm—diamond, $FeCO_{3\ liq}$—melt of almost $FeCO_3$ composition, HM—hematite–magnetite buffer, CCO—C-CO buffer, MW—magnetite–wüstite buffer, IW—iron-wüstite buffer.

4.2. Indicators of an Effect of C-, S-, Fe-Enriched Melts and Fluids on Upper Mantle Rocks on a Base of Experimental Results in Simplified Olivine–Siderite–Sulfur System

A detailed study of phase relationships in the obtained samples revealed key indicator characteristics of mineral and melt phases formed during the interaction of Fe,Ni–olivine and siderite with sulfur melt. Specifically, it was established that the main indicators of Fe,Ni–olivine sulfidation are polycrystalline aggregates of orthopyroxene and pyrrhotite, inheriting the shape of various sections of olivine crystals with a rhomboprismatic habit. Orthopyroxene crystals with complex zoning (based on FeO content) and pyrrhotite inclusions can also be classified as these indicators. To our knowledge, there are some findings among inclusions containing similar assemblage in natural diamonds [52]: enstatite + olivine + pyrrhotite + pentlandite.

Aggregates of pyrrhotite and ferromagnesite, often characterized by a hexagonal shape (siderite crystal cross-section), can be considered indicators of siderite sulfidation. These include pyrrhotite with ferromagnesite rims, pyrrhotite with ferromagnesite inclusions, and ferromagnesite containing magnetite–pyrrhotite inclusions. Similar inclusions ("magnetite 'crowns' on pyrrhotite") have been identified in natural diamond [53]; authors suggest that magnetite is a reaction product of a carbonate-containing fluid with a sulfide melt. Moreover, inclusions of magnetite + magnesite assemblage in diamond were also described [51].

Previously, we experimentally studied interactions in olivine–magnesite–sulfur, olivine–ankerite–sulfur, and olivine–ankerite–pyrite systems, simulating metasomatic transformations of carbonate–silicate associations (including their sulfidation) under the influence of sulfur-enriched melts/fluids [19,20], and identified indicators of these processes. The bulk compositions of the systems and the initial material weights are presented in Tables 1 and 2. The experimental results (phase composition of the obtained samples) are shown in Table 3.

We believe it is relevant to compare the obtained results using indicator characteristics of processes in systems with different carbonates for the following reasons. The most common alkaline earth carbonates in modern marine sediments and in hydrothermally altered basalt are calcite/aragonite $CaCO_3$, dolomite $CaMg(CO_3)_2$ [54], and magnesite $MgCO_3$ [15]. It has been experimentally demonstrated [55–57] that the contents of magnesium, calcium, and strontium and their ratios in Phanerozoic seawater have varied over time. Moreover, if we consider the evolution of sediments on a timescale of billions of years, ancient Precambrian carbonates were enriched in iron and manganese compared to Phanerozoic ones [58–60]. It has been established that polycrystalline aggregates of low- or iron-free orthopyroxene and pyrite, as well as zoned olivine crystals with an FeO-rich center and a magnesian peripheral part containing sulfide inclusions, serve as indicators of the interaction of olivine and magnesite with sulfur melt at P,T parameters of the lithospheric mantle [19]. In the case of olivine and ankerite interactions with sulfur melt [20], indicators of parallel sulfidation processes of olivine and ankerite are (1) polycrystalline aggregates of diopside, alkaline earth carbonates, and pyrite, (2) the zonal structure of olivine crystals with an FeO-rich central zone and magnesian (nickel-free and iron-free) periphery, and (3) the formation of pyrite, pyrrhotite, and clinopyroxene inclusions in virtually iron-free, nickel-free olivine.

Thus, the obtained experimental data demonstrated significant differences in the indicator characteristics of the interaction processes of magnesite, ankerite, and siderite with Fe,Ni–olivine and sulfur-enriched melt/fluid, which can be used to reconstruct either experimental results in carbonate-sulfide or carbonate-silicate-sulfide systems or natural metasomatic processes in modern and ancient subduction zones (with some limitations).

5. Conclusions

- Experimental modeling of the interaction processes of C-, S-, Fe-enriched metasomatic agents with upper mantle rocks, under Archean subduction geotherm has been performed in in the simplified olivine–siderite–sulfur system. It was shown that the interaction of Fe,Ni–olivine and siderite with sulfur melt leads to the formation of an pyrrhotite + orthopyroxene + ferromagnesite ± magnetite assemblage (1150–1250 °C), generation of sulfide (1350 °C) and carbonate–silicate melts (1350–1450 °C), as well as to the dissolution of diamond seed crystals.
- It has been experimentally demonstrated that the main interaction processes in the simplified olivine–siderite–sulfur system (6.3 GPa, 1150–1450 °C, 20–60 h) are the sulfidation of Fe,Ni–olivine and siderite, including the recrystallization of olivine

and siderite in sulfur melt, the extraction of iron and nickel into the melt, and the subsequent formation of newly formed sulfides, orthopyroxene and ferromagnesite, as well as the redox dissociation of siderite with the formation of magnetite, and inferred formation of C^0 and oxidized (oxygen-rich) fluid.

- It has been proposed that the main indicators of an effect of C-, S-, Fe-enriched melts and fluids on upper mantle rocks are the obtained (1) polycrystalline aggregates of orthopyroxene + pyrrhotite, as well as pyrrhotite + ferromagnesite, inheriting the shape of olivine crystals of rhomboprismatic habit and rhombohedral siderite crystals, respectively; (2) orthopyroxene crystals with complex zoning (by FeO content) and with pyrrhotite inclusions; (3) pyrrhotite with ferromagnesite inclusions, as well as ferromagnesite containing two-phase inclusions of magnetite + pyrrhotite.
- The processes of mantle metasomatism involving carbon- and sulfur-bearing agents, potentially possible under conditions of early subduction of Fe-rich carbonate- and sulfide-bearing Archean sedimentary rocks, have been experimentally realized and studied. The obtained data with some limitations can be used to construct models of metasomatism in the Mesoarchean-Paleoproterozoic, as well as to study the geochemical cycles of carbon, iron, and sulfur in the history of the Earth.

Author Contributions: Conceptualization, Y.N.P. and Y.V.B.; methodology, Y.N.P.; validation, Y.N.P. and Y.V.B.; formal analysis, Y.V.B.; investigation, Y.V.B.; resources, Y.N.P.; data curation, Y.V.B.; writing—original draft preparation, Y.V.B.; writing—review and editing, Y.N.P.; visualization, Y.V.B.; supervision, Y.N.P.; project administration, Y.V.B.; funding acquisition, Y.N.P. All authors have read and agreed to the published version of the manuscript.

Funding: This research was funded by the Russian Science Foundation, grant number 24-17-00032 (https://rscf.ru/project/24-17-00032/ (accessed on 8 August 2026)).

Data Availability Statement: The original data presented in the study are openly available in Mendeley Data at: https://doi.org/10.17632/tk67zczsb3.1.

Acknowledgments: We thank A. F. Khokhryakov for providing the samples of natural siderite.

Conflicts of Interest: The authors declare no conflicts of interest. The funders had no role in the design of the study; in the collection, analyses, or interpretation of data; in the writing of the manuscript; or in the decision to publish the results.

References

1. Smit, K.V.; Shirey, S.B.; Hauri, E.H.; Stern, R.A. Sulfur isotopes in diamonds reveal differences in continent construction. *Science* **2019**, *364*, 383–385. [CrossRef] [PubMed]
2. Gurney, J.J.; Helmstaedt, H.H.; Richardson, S.H.; Shirey, S.B. Diamonds through Time. *Econ. Geol.* **2010**, *105*, 689–712. [CrossRef]
3. Shirey, S.B.; Harris, J.; Richardson, S.H.; Fouch, M.J.; James, D.E.; Cartigny, P.; Deines, P.; Viljoen, F. Diamond genesis, seismic structure, and evolution of the Kaapvaal-Zimbabwe craton. *Science* **2002**, *297*, 1683–1686. [CrossRef] [PubMed]
4. Klein, C. Some Precambrian Banded Iron-Formations (BIFs) from around the World: Their Age, Geologic Setting, Mineralogy, Metamorphism, Geochemistry and Origin. *Am. Mineral.* **2005**, *90*, 1473–1499. [CrossRef]
5. Konhauser, K.O.; Amskold, L.; Lalonde, S.V.; Posth, N.R.; Kappler, A.; Anbar, A. Decoupling photochemical Fe(II) oxidation from shallow-water BIF deposition Decoupling photochemical Fe(II) oxidation from shallow-water BIF deposition. *Earth Planet. Sci. Lett.* **2007**, *258*, 87–100. [CrossRef]
6. Horstmann, U.E.; Hälbich, I.W. Chemical composition of banded iron-formations of the Griqualand West Sequence, Northern Cape Province, South Africa, in comparison with other Precambrian iron formations. *Precambrian Res.* **1995**, *72*, 109–145. [CrossRef]
7. Beukes, N.J.; Gutzmer, J. Origin and paleoenvironmental significance of major iron formations at the Archean–Paleoproterozoic Boundary. *Rev. Econ. Geol. Banded Iron Form.-Relat. High-Grade Iron Ore* **2008**, *15*, 5–47. [CrossRef]
8. Walker, J.C. Suboxic diagenesis in banded iron formations. *Nature* **1984**, *309*, 340–342. [CrossRef] [PubMed]
9. Webb, A.D.; Dickens, G.R.; Oliver, N.H. From banded iron-formation to iron ore: Geochemical and mineralogical constraints from across the Hamersley Province, Western Australia. *Chem. Geol.* **2003**, *197*, 215–251. [CrossRef]

10. Bowins, R.J.; Crocket, J.H. Sulfur and carbon isotopes in Archean banded iron formations: Implications for sulfur sources. *Chem. Geol.* **1994**, *111*, 307–323. [CrossRef]
11. Farquhar, J.; Wing, B.A.; Mckeegan, K.D.; Harris, J.W.; Cartigny, P.; Thiemens, M.H. Mass-independent sulfur of inclusions in diamond and sulfur recycling on early Earth. *Science* **2002**, *298*, 2369–2372. [CrossRef] [PubMed]
12. Kang, N.; Schmidt, M.W. The melting of subducted banded iron formations. *Earth Planet. Sci. Lett.* **2017**, *476*, 165–178. [CrossRef]
13. Thode, H.G.; Goodwin, A.M. Further sulfur and carbon isotope studies of late Archean iron-formations of the Canadian shield and the rise of sulfate reducing bacteria. *Precambrian Res.* **1983**, *20*, 337–356. [CrossRef]
14. Diekrup, D.; Hannington, M.D.; Strauss, H.; Ginley, S.J. Decoupling of Neoarchean sulfur sources recorded in Algoma-type banded iron formation. *Earth Planet. Sci. Lett.* **2018**, *489*, 1–7. [CrossRef]
15. Evans, K.A.; Powell, R. The effect of subduction on the sulphur, carbon and redox budget of lithospheric mantle. *J. Metamorph. Geol.* **2015**, *33*, 649–670. [CrossRef]
16. Komiya, T.; Hayashi, M.; Maruyama, S.; Yurimoto, H. Intermediate-P/T type Archean metamorphism of the Isua supracrustal belt: Implications for secular change of geothermal gradients at subduction zones and for Archean plate tectonics. *Am. J. Sci.* **2002**, *302*, 806–826. [CrossRef]
17. Sizova, E.; Gerya, T.; Brown, M.; Perchuk, L.L. Subduction styles in the Precambrian: Insight from numerical experiments. *Lithos* **2010**, *116*, 209–229. [CrossRef]
18. Santosh, M.; Maruyama, S.; Komiya, T.; Yamamoto, S. Orogens in the evolving Earth: From surface continents to 'lost continents' at the core–mantle boundary. In *The Evolving Continents: Understanding Processes of Continental Growth*; Kusky, T.M., Zhai, M.-G., Xiao, W., Eds.; Geological Society: London, UK; Special Publications: London, UK, 2010; Volume 338, pp. 77–116.
19. Bataleva, Y.V.; Palyanov, Y.N.; Borzdov, Y.M.; Zdrokov, E.V.; Sobolev, N.V. Experimental modeling of the interaction of subducted carbonates and sulfur with mantle silicates. *Dokl. Earth Sci.* **2016**, *470*, 953–956. [CrossRef]
20. Zdrokov, E.; Novoselov, I.; Bataleva, Y.; Borzdov, Y.; Palyanov, Y. Experimental modeling of silicate and carbonate sulphidation under lithospheric mantle P,T-parameters. *Minerals* **2019**, *9*, 425. [CrossRef]
21. Gaul, O.F.; Griffin, W.L.; O'Reilly, S.Y.; Pearson, N.J. Mapping olivine composition in the lithospheric mantle. *Earth Planet. Sci. Lett.* **2000**, *182*, 223–235. [CrossRef]
22. Stachel, T.; Banas, A.; Muehlenbachs, K.; Kurszlaukis, S.; Walker, E.C. Archean diamonds from Wawa (Canada): Samples from deep cratonic roots predating cratonization of the Superior Province. *Contrib. Mineral. Petrol.* **2006**, *151*, 737–750. [CrossRef]
23. Bernstein, S.; Kelemen, P.B.; Hanghøj, K. Consistent olivine Mg# in cratonic mantle reflects Archean mantle melting to the exhaustion of orthopyroxene. *Geology* **2007**, *35*, 459–462. [CrossRef]
24. Griffin, W.L.; O'Reilly, S.Y.; Abe, N.; Aulbach, S.; Davies, R.M.; Pearson, N.J.; Doyle, B.J.; Kivi, K. The origin and evolution of Archean lithospheric mantle. *Precambrian Res.* **2003**, *127*, 19–41. [CrossRef]
25. Palyanov, Y.N.; Kupriyanov, I.N.; Khokhryakov, A.F.; Borzdov, Y.M. High-pressure crystallization and properties of diamond from magnesium-based catalysts. *CrystEngComm* **2017**, *19*, 4459–4475. [CrossRef]
26. Sokol, A.G.; Borzdov, Y.M.; Palyanov, Y.N.; Khokhryakov, A.F. High-temperature calibration of a multi-anvil high pressure apparatus. *High Press. Res.* **2015**, *35*, 139–147. [CrossRef]
27. Palyanov, Y.N.; Sokol, A.G. The effect of composition of mantle fluid/melts on diamond formation processes. *Lithos* **2009**, *112S*, 690–700. [CrossRef]
28. Pal'yanov, Y.N.; Sokol, A.G.; Borzdov, Y.M.; Khokhryakov, A.F. Fluid-bearing alkaline-carbonate melts as the medium for the formation of diamonds in the Earth's mantle: An experimental study. *Lithos* **2002**, *60*, 145–159. [CrossRef]
29. Day, H.W. A revised diamond–graphite transition curve. *Am. Mineral.* **2012**, *97*, 52–62. [CrossRef]
30. Kennedy, C.S.; Kennedy, G.C. The equilibrium boundary between graphite and diamond. *J. Geophys. Res.* **1976**, *81*, 2467–2470. [CrossRef]
31. Palyanov, Y.N.; Borzdov, Y.M.; Bataleva, Y.V.; Sokol, A.G.; Palyanova, G.A.; Kupriyanov, I.N. Reducing role of sulfides and diamond formation in the Earth's mantle. *Earth Planet. Sci. Lett.* **2007**, *260*, 242–256. [CrossRef]
32. Ulmer, P.; Sweeney, R.J. Generation and differentiation of group II kimberlites: Constraints from a highpressure experimental study to 10 GPa. *Geochim. Cosmochim. Acta* **2002**, *66*, 2139–2153. [CrossRef]
33. Brey, G.P.; Bulatov, V.K.; Girnis, A.V.; Lahaye, Y. Experimental melting of carbonated peridotite at 6–10 GPa. *J. Petrol.* **2008**, *49*, 797–821. [CrossRef]
34. Brey, G.P.; Bulatov, V.K.; Girnis, A.V. Influence of water and fluorine on melting of carbonated peridotite at 6 and 10 GPa. *Lithos* **2009**, *112*, 249–259. [CrossRef]
35. Frank, F.C.; Puttick, K.E.; Wilks, E.M. Etch pits and trigons on diamond: I. *Philos. Mag.* **1958**, *3*, 1262–1272. [CrossRef]
36. Brazhkin, V.V.; Popova, S.V.; Voloshin, R.N. Pressure-temperature phase diagram of molten elements: Selenium, sulfur and iodine. *Phys. B Condens. Matter.* **1999**, *265*, 64–71. [CrossRef]
37. Bataleva, Y.V.; Palyanov, Y.N.; Borzdov, Y.M.; Sobolev, N.V. Sulfidation of silicate mantle by reduced S-bearing metasomatic fluids melts. *Geology* **2016**, *44*, 271–274. [CrossRef]

38. Kang, N.; Schmidt, M.W.; Poli, S.; Franzolin, E.; Connolly, J.A.D. Melting of siderite to 20 GPa and thermodynamic properties of FeCO3-melt. *Chem. Geol.* **2015**, *400*, 34–43. [CrossRef]
39. Tao, R.; Fei, Y.; Zhang, L. Experimental determination of siderite stability at high pressure. *Am. Mineral.* **2013**, *98*, 1565–1572. [CrossRef]
40. Prinz, M.; Manson, D.V.; Hlava, P.F.; Keil, K. Inclusions in diamonds: Garnet lherzolite and eclogite assemblages. *Phys. Chem. Earth* **1975**, *9*, 797–815. [CrossRef]
41. Sobolev, N.V.; Yefimova, E.S.; Channer, D.M.D.; Anderson, P.F.N.; Barron, K.M. Unusual upper mantle beneath Guaniamo, Guyana shield: Evidence from diamond inclusions. *Geology* **1998**, *26*, 971–974. [CrossRef]
42. Stachel, T.; Harris, J.W.; Brey, G.P. Rare and unusual mineral inclusions in diamonds from Mwadui, Tanzania. *Contrib. Mineral. Petrol.* **1998**, *132*, 34–47. [CrossRef]
43. Runge, E.A.; Mansor, M.; Shuster, J.; Fischer, S.; Liu, Y.; Lunter, D.J.; Kappler, A.; Duda, J.-P. Sulfidation of nano-magnetite to pyrite: Implications for interpreting paleoenvironmental proxies and biosignature records in hydrothermal sulfide deposits. *Earth Planet. Sci. Lett.* **2023**, *617*, 118261. [CrossRef]
44. Shatskiy, A.; Borzdov, Y.M.; Litasov, K.D.; Kupriyanov, I.N.; Ohtani, E.; Palyanov, Y.N. Phase relations in the system FeCO3-CaCO3 at 6 GPa and 900–1700 °C and its relation to the system CaCO3-FeCO3-MgCO3. *Am. Mineral.* **2014**, *99*, 773–785. [CrossRef]
45. Matjuschkin, V.; Blundy, J.D.; Brooker, R.A. The effect of pressure on sulphur speciation in mid-to deep-crustal arc magmas and implications for the formation of porphyry copper deposits. *Contrib. Mineral. Petrol.* **2016**, *171*, 66. [CrossRef]
46. Palyanov, Y.N.; Borzdov, Y.M.; Khokhryakov, A.F.; Bataleva, Y.V.; Kupriyanov, I.N. Effect of sulfur on diamond growth and morphology in metal–carbon systems. *CrystEngComm* **2020**, *22*, 5497–5508. [CrossRef]
47. Litvin, Y.A.; Shushkanova, A.V.; Zharikov, V.A. Immiscibility of sulfide-silicate melts in the mantle: Role in the syngenesis of diamond and inclusions (Based on experiments at 7.0 GPa). *Dokl. Earth Sci.* **2005**, *403*, 719–722.
48. Luth, R.W.; Palyanov, Y.N.; Bureau, H. Experimental petrology applied to natural diamond growth. *Rev. Mineral. Geochem.* **2022**, *88*, 755–808. [CrossRef]
49. Palyanov, Y.u.N.; Borzdov, Y.u.M.; Khokhryakov, A.F.; Kupriyanov, I.N.; Sobolev, N.V. Sulfide melts–graphite interaction at HPHT conditions: Implications for diamond genesis. *Earth Planet. Sci. Lett.* **2006**, *250*, 269–280. [CrossRef]
50. Sokol, A.G.; Pal'yanov, Y.N. Diamond formation in the system MgO–SiO2–H2O–C at 7.5 GPa and 1600 °C. *Contrib. Mineral. Petrol.* **2008**, *155*, 33–43. [CrossRef]
51. Novoselov, I.D.; Ivanov, S.V.; Bataleva, Y.u.N.; Palyanov, Y.u.N. Experimental modeling of interaction of eclogitic and lherzolitic garnets with sulfur-rich fluids under lithospheric mantle P,T-parameters. *Russ. Geol. Geophys.* **2026**, *in press*. [CrossRef]
52. Pantaleo, N.S.; Newton, M.G.; Gogineni, S.V.; Melton, C.E.; Giardini, A.A. Mineral inclusions in four Arkansas diamonds; their nature and significance. *Am. Miner.* **1979**, *64*, 1059–1062.
53. Jacob, D.E.; Piazolo, S.; Schreiber, A.; Trimby, P. Redox-freezing and nucleation of diamond via magnetite formation in the Earth's mantle. *Nat. Commun.* **2016**, *7*, 11891. [CrossRef] [PubMed]
54. Mackenzie, F.T.; Morse, J.W. Sedimentary carbonates through Phanerozoic time. *Geochim. Cosmochim. Acta* **1992**, *56*, 3281–3295. [CrossRef]
55. Horita, J.; Friedman, T.J.; Lazar, B.; Holland, H.D. The composition of Permian seawater. *Geochim. Cosmochim. Acta* **1991**, *55*, 417–432. [CrossRef] [PubMed]
56. Horita, J.; Zimmermann, H.; Holland, H. Chemical evolution of seawater during the Phanerozoic: Implications from the record of marine evaporates. *Geochim. Cosmochim. Acta* **2002**, *66*, 3733–3756.
57. Lowenstein, T.K.; Timofeeff, M.N.; Brennan, S.T.; Hardie, L.A.; Demicco, R.V. Oscillations in Phanerozoic seawater chemistry: Evidence from fluid inclusions. *Science* **2001**, *294*, 1086–1088. [CrossRef] [PubMed]
58. Brand, U.; Veizer, J. Chemical diagenesis of a multicomponent carbonate system: I. Trace elements. *J. Sediment. Petrol.* **1980**, *50*, 1219–1236. [CrossRef]
59. Veizer, J. Carbonates and ancient oceans: Isotopic and chemical record on time scales of 107–109 years. *Geophys. Monogr. Ser.* **1985**, *32*, 595–601.
60. Veizer, J. Trace elements and isotopes in sedimentary carbonates. *Rev. Mineral.* **1983**, *11*, 265–300. [CrossRef]

Disclaimer/Publisher's Note: The statements, opinions and data contained in all publications are solely those of the individual author(s) and contributor(s) and not of MDPI and/or the editor(s). MDPI and/or the editor(s) disclaim responsibility for any injury to people or property resulting from any ideas, methods, instructions or products referred to in the content.